[AMERICAN JOURNAL OF SCIENCE, VOL. 296, MARCH, 1996, P. 197–243]

American Journal of Science

MARCH 1996

CYCLING OF IRON AND MANGANESE IN SURFACE SEDIMENTS: A GENERAL THEORY FOR THE COUPLED TRANSPORT AND REACTION OF CARBON, OXYGEN, NITROGEN, SULFUR, IRON, AND MANGANESE

PHILIPPE VAN CAPPELLEN and YIFENG WANG
School of Earth and Atmospheric Sciences,
Georgia Institute of Technology,
Atlanta, Georgia 30332

ABSTRACT. This paper presents a multicomponent early diagenetic model which explicitly accounts for the coupling of the redox cycles of Fe and Mn to those of oxygen, carbon, sulfur, and nitrogen. Rate expressions are used to represent the oxidation of organic carbon, the oxidation of secondary reduced species formed as byproducts of organic matter oxidation, and the precipitation and dissolution of sulfide and carbonate minerals. The net rate of organic carbon oxidation is broken down into the contributions of aerobic respiration, denitrification, dissimilatory Mn(IV) reduction, dissimilatory Fe(III) reduction, sulfate reduction, and methanogenesis. The computational algorithm is based on a modified Monod kinetics formulation for the organic matter degradation pathways. The non-specific adsorption of ammonia, the surface complexation of Fe^{2+} and Mn^{2+} cations, and the homogeneous interconversions within the dissolved carbonate-sulfide system are treated as equilibrium reactions. The transport processes included are sediment advection, pore water diffusion, and particle mixing and irrigation by benthic macrofauna. Chemical component concentrations and pore water alkalinity are described by a set of continuity equations characterized by nonlinear reaction rate terms. The equations are solved by finite-difference. The distribution of pore water pH is derived from the calculated profiles of total dissolved inorganic carbon, total dissolved sulfide, and alkalinity. Particulate deposition fluxes and bottom water composition are imposed as upper boundary conditions.

The model is applied to an extensive set of data collected in a marine sediment from the Skagerrak (Denmark). Theoretical depth profiles reproduce the measured pore water concentrations of O_2, NO_3^-, NH_4^+, Mn^{2+}, and Fe^{2+} plus the solid sediment concentrations of Fe(III), Mn(IV), sulfide-bound Fe(II), and non-sulfide Fe(II). The model also correctly simulates the depth distribution of measured sulfate reduction rates. According to the computations, approximately two thirds of the total rate of iron reduction in the sediment are utilized directly by bacteria to oxidize organic carbon (dissimilatory Fe reduction). Manganese reduction, on the other hand, is mostly due to chemical reaction with dissolved Fe^{2+}. Despite the relatively high rates of iron and manganese reduction, only very small amounts of the Fe(II) and

Mn(II) produced during early diagenesis are permanently buried in the deeper sediment. Most of the dissolved and solid-bound Fe(II) and Mn(II) cations reoxidize in the surface sediment or escape to the water column. The main oxidation pathways in the sediment are heterogeneous oxygenation of surface complexed Fe^{2+} and Mn^{2+} cations. The model also predicts that intense redox cycling of Fe and Mn should cause the appearance of a pH minimum at the base of the aerobic surface layer.

INTRODUCTION

The transformations of iron and manganese are key processes in the biogeochemistry of marine and freshwater sediments. The oxides and oxyhydroxides (henceforth referred to as (hydr)oxides) of iron and manganese reductively dissolve upon burial or mixing below the aerobic surface layer of sediments underlying oxygenated bottom waters. Pore water Fe(II) and Mn(II) produced within the anaerobic zone may adsorb onto sediment particles, (co)precipitate as authigenic sulfide, carbonate, and phosphate mineral phases, or be transported back toward the water-sediment interface via pore water diffusion and irrigation. A fraction of the particle-bound Fe(II) and Mn(II) may also be returned to the oxidized surface layer of the sediment through particle mixing induced by benthic macrofaunal activity. Upon encountering more oxidizing conditions, the reduced Fe(II) and Mn(II) reoxidize and precipitate as (hydr)oxides.

The coupling of redox transformations and transport processes gives rise to the cycling of iron and manganese between the aerobic and anaerobic portions of surface sediments. An iron or manganese cation deposited at the water-sediment interface may cycle many times through its oxidized and reduced states before being buried permanently below the zone of active early diagenesis. Consequently, the electron fluxes associated with the iron and manganese cycles in a sediment may greatly exceed the electron acceptor capacities supplied by deposition of Fe and Mn (hydr)oxides from the oxygenated water column. The redox cycling of iron and manganese also plays an important role in the early diagenetic behavior of numerous other elements, including phosphorus and trace metals (Froelich and others, 1979; Krom and Berner, 1981; Shimmield and Pedersen, 1990).

The general outline of the early diagenetic redox cycles of iron and manganese given above has been known for many years (Lynn and Bonatti, 1965). Recent work, however, has revealed that the cycles are much more complex than previously envisioned (Canfield, Thamdrup, and Hansen, 1993; Aller, 1994). In particular, it is now clearly established that the reduction and oxidation of iron and manganese in natural aquatic systems may proceed via a variety of pathways. Microorganisms can couple the reduction of iron and manganese (hydr)oxides directly to organic matter oxidation (Lovley, 1987, 1991; Nealson and Myers, 1992; Burdige, 1993; DiChristina and DeLong, 1993). Dissimilatory iron and manganese reduction, however, compete with the chemical reduction of

the (hydr)oxides by a variety of inorganic and organic reductants (Berner, 1970; Postma, 1985; Stone, 1987; Wehrli, Sulzberger, and Stumm, 1989; Luther and others, 1992; Sunda and Kieber, 1994). Manganese (hydr)oxides, for instance, may be reduced by pore water Fe^{2+} (Postma, 1985; Myers and Nealson, 1988; Burdige, Dhakar, and Nealson, 1992), while both iron and manganese (hydr)oxides are reductively dissolved through reaction with sulfide (Pyzik and Sommer, 1981; Burdige and Nealson, 1986; Canfield and Berner, 1987; Yao and Millero, 1993). Similarly, a variety of microbial and abiotic oxidation pathways of reduced iron and manganese species have been documented in natural aquatic environments (Sung and Morgan, 1980; Davison and Seed, 1983; Emerson and others, 1982; Sunda and Huntsman, 1990; Luther and others, 1992; Stumm and Sulzberger, 1992).

Previously published models of early diagenesis have not, to our knowledge, explored the possibility of multiple pathways of oxidation and reduction of Fe and Mn in sediments. Existing models of manganese or iron cycling capture the oxidation or reduction of the metal in a single rate expression. Furthermore, it has been commonly assumed that the rate laws describing oxidation and reduction depend only on the concentrations of the reduced and oxidized forms of the metal itself or obey *a priori* imposed depth distributions (Michard, 1971; Robbins and Callender, 1975; Burdige and Gieskes, 1983; Gratton and others, 1990; Wersin and others, 1991). With these assumptions, the conservation equations of the metal species can be solved independently from the distributions of other chemical elements. However, it also means that the models are limited in their ability to simulate the coupled, multicomponent chemical dynamics of early diagenetic systems. In this respect, the models of Aller (1990) and Rabouille and Gaillard (1991) represent a step forward, because they link the redox transformations of manganese to those of organic carbon and oxygen.

In this paper, we extend the earlier theoretical work by developing a transport-reaction model that explicitly accounts for the coupling of the redox cycles of iron, manganese, oxygen, carbon, sulfur, and nitrogen. The model solves simultaneously the continuity equations representing mass conservation of all the independent reactive chemical species involved in controlling the spatial and temporal distributions of iron and manganese (table 1). Each individual reaction pathway that produces or consumes reactive species is included in the appropriate conservation equations, either as a rate expression or, for very fast reactions, as an equilibrium constraint. The equations of the independent species must be solved together, because they are coupled through the reaction rate terms. The result is an early diagenetic model in which the downward succession of reaction zones comes about naturally as the result of the production, consumption, and transport of all reactive species. There is no longer a need to assign beforehand the depth distribution of chemical conditions in the sediment in order to predict the distributions of iron and manganese.

TABLE 1

Dissolved, interfacial and solid species included in the model. $\equiv S - H^0$ corresponds to a hydrated surface site. The chemical formula used to represent sedimentary organic matter assumes an average oxidation state of zero for organic carbon

Dissolved species	O_2
	NO_3^-
	Mn^{2+}
	Fe^{2+}
	SO_4^{2-}
	NH_4^+
	CH_4
	$CO_2(aq).\ HCO_3^-.\ CO_3^{2-}$
	$H_2S.\ HS^-$
	H^+
Interfacial species	$\equiv S - H^0$
	$\equiv S - Mn^+$
	$\equiv S - Fe^+$
	$NH_4^+(ads)$
Solid species	$(CH_2O)_x(NH_3)_y(H_3PO_4)_z$
	MnO_2
	$Fe(OH)_3$
	$Ca_{1-x_{Mn}}Mn_{x_{Mn}}CO_3$
	$Ca_{1-x_{Fe}}Fe_{x_{Fe}}CO_3$
	FeS

REACTIVE SPECIES

The first step in constructing the early diagenetic model for iron and manganese is the choice of the reactive chemical species (table 1). The species include the various dissolved, interfacial, and solid forms of the metals themselves, as well as other pore water and particulate constituents that affect the rates and loci of production and consumption of Fe and Mn species in the sediment.

In contrast to earlier models, adsorbed iron and manganese cations are included as separate species in our model. Interfacial Fe(II) and Mn(II) are critical reaction intermediates in the oxidative transformations of the metals (Morgan, Sung, and Stone, 1985). Furthermore, adsorbed Fe(II) and Mn(II) may represent significant fractions of solid-bound metals in surface sediments (Murray, Balistrieri, and Paul, 1984; Canfield, Thamdrup, and Hansen, 1993; this work).

The solid phases $Fe(OH)_3$ and MnO_2 are used as idealized representations of the reactive, bioavailable fractions of oxidized iron and manganese (hydr)oxides. Iron monosulfide, FeS, is the initial Fe(II) sulfide precipitate forming in anoxic sediments as the result of sulfate reduction (Berner, 1984). The kinetically-favored FeS is used in the model because it controls pore water iron concentrations in sulfide-producing sediments, rather than the thermodynamically more stable pyrite (Boudreau

and Canfield, 1988). Carbonate alkalinity production during anaerobic respiration may lead to the precipitation of carbonate minerals. In freshwater sediments, relatively pure $FeCO_3$ and $MnCO_3$ may form (Emerson, 1976; Wersin and others, 1991). In marine depositional environments, however, the formation of solid solutions with $CaCO_3$ is more likely, especially for Mn(II) (Pedersen and Price, 1982; Mucci, 1988; Jakobsen and Postma, 1989; Gaillard, Pauwels, and Michard, 1989).

With the exception of particulate organic matter and adsorbed ammonia, the remaining species in table 1 are solutes. They correspond to the principal redox and acid-base species found in natural pore waters. Typically, the vertical profiles of these species are used to define the distribution of geochemical zones in sediments (Froelich and others, 1979).

The set of reactive species in table 1 offers a simplified description of the composition of sediments and pore waters. Nonetheless, it does provide the model with the essential actors needed to simulate at a fairly realistic level the chemical complexity of early diagenetic systems. Furthermore, it is important to note that the modeling approach adopted here is completely general and that, in theory, there is no limit to the number of species and reactions that can be included.

REACTIONS

Most biogeochemical transformations affecting iron and manganese in surface sediments are driven, directly or indirectly, by the decomposition of organic matter. The supply of organic detritus from the water column is the ultimate source of energy for the microbial and macrofaunal populations that inhabit a surface sediment. (Note: for sediments situated within the photic zone, organic matter supply may also originate from benthic primary production.) This external supply of metabolic energy maintains the overall state of thermodynamic disequilibrium of the surface sediment which is expressed, among other things, by the persistence of vertical gradients in chemical and biological properties.

The decomposition of organic matter is the result of many enzymatic reactions involving a variety of organisms and a variety of intermediate compounds. However, the net effect of organic matter decomposition on pore water and solid sediment composition can be represented by overall reactions (Van Cappellen, Gaillard, and Rabouille, 1993). The idealized net decomposition reactions included in the model are listed in table 2. They include oxic respiration (eq 1), denitrification (eq 2), manganese (hydr)oxide reduction (eq 3), iron (hydr)oxide reduction (eq 4), sulfate reduction (eq 5), and methanogenesis (eq 6). The reactions are listed roughly in the sequence in which they occur with increasing depth in a sediment. The sequence reflects the order of decreasing energy yield of the oxidation reactions (Berner, 1980).

Reactions (1) to (6) are termed the primary redox reactions with organic carbon acting as the reductant. The oxidation of organic matter

TABLE 2

Biogeochemical reactions included in the model

Primary redox reactions:

$$(CH_2O)_x(NH_3)_y(H_3PO_4)_z + (x + 2y)O_2 + (y + 2z)HCO_3^- \xrightarrow{R_1/x} (x + y + 2z)CO_2 + yNO_3^- + zHPO_4^{2-} + (x + 2y + 2z)H_2O \quad (1)$$

$$(CH_2O)_x(NH_3)_y(H_3PO_4)_z + \left(\frac{4x + 3y}{5}\right)NO_3^- \xrightarrow{R_2/x} \left(\frac{2x + 4y}{5}\right)N_2 + \left(\frac{x - 3y + 10x}{5}\right)CO_2 + \left(\frac{4x + 3y - 10z}{5}\right)HCO_3^- + zHPO_4^{2-} + \left(\frac{3x + 6y + 10z}{5}\right)H_2O \quad (2)$$

$$(CH_2O)_x(NH_3)_y(H_3PO_4)_z + 2xMnO_2 + (3x + y - 2z)CO_2 + (x + y - 2z)H_2O \xrightarrow{R_3/x} 2xMn^{2+} + (4x + y - 2z)HCO_3^- + yNH_4^+ + zHPO_4^{2-} \quad (3)$$

$$(CH_2O)_x(NH_3)_y(H_3PO_4)_z + 4xFe(OH)_3 + (7x + y - 2z)CO_2 \xrightarrow{R_4/x} 4xFe^{2+} + (8x + y - 2z)HCO_3^- + yNH_4^+ + zHPO_4^{2-} + (3x - y + 2z)H_2O \quad (4)$$

$$(CH_2O)_x(NH_3)_y(H_3PO_4)_z + \frac{x}{2}SO_4^{2-} + (y - 2z)CO_2 + (y - 2z)H_2O \xrightarrow{R_5/x} \frac{x}{2}H_2S + (x + y - 2z)HCO_3^- + yNH_4^+ + zHPO_4^{2-} \quad (5)$$

$$(CH_2O)_x(NH_3)_y(H_3PO_4)_z + (y - 2z)H_2O \xrightarrow{R_6/x} \frac{x}{2}CH_4 + \left(\frac{x - 2y + 4z}{2}\right)CO_2 + (y - 2z)HCO_3^- + yNH_4^+ + zHPO_4^{2-} \quad (6)$$

Secondary redox reactions:

$$\equiv S - Mn^+ + \frac{1}{2}O_2 + HCO_3^- \xrightarrow{R_7} \equiv S - H^0 + MnO_2 + CO_2 \quad (7)$$

$$Fe^{2+} + \frac{1}{4}O_2 + 2HCO_3^- + \frac{1}{2}H_2O \xrightarrow{R_8} Fe(OH)_3 + 2CO_2 \quad (8)$$

$$\equiv S - Fe^+ + \frac{1}{4}O_2 + HCO_3^- + \frac{3}{2}H_2O \xrightarrow{R_9} \equiv S - H^0 + Fe(OH)_3 + CO_2 \quad (9)$$

$$2Fe^{2+} + MnO_2 + 2HCO_3^- + 2H_2O \xrightarrow{R_{10}} 2Fe(OH)_3 + Mn^{2+} + 2CO_2 \quad (10)$$

$$NH_4^+ + 2O_2 + 2HCO_3^- \xrightarrow{R_{11}} NO_3^- + 2CO_2 + 3H_2O \quad (11)$$

$$H_2S + 2O_2 + 2HCO_3^- \xrightarrow{R_{12}} SO_4^{2-} + 2CO_2 + 2H_2O \quad (12)$$

$$H_2S + 2CO_2 + MnO_2 \xrightarrow{R_{13}} Mn^{2+} + S^0 + 2HCO_3^- \quad (13)$$

$$H_2S + 4CO_2 + 2Fe(OH)_3 \xrightarrow{R_{14}} 2Fe^{2+} + S^0 + 4HCO_3^- + 2H_2O \quad (14)$$

TABLE 2
(continued)

$$FeS + 2O_2 \xrightarrow{R_{15}} Fe^{2+} + SO_4^{2-} \quad (15)$$

$$CH_4 + 2O_2 \xrightarrow{R_{16}} CO_2 + 2H_2O \quad (16)$$

$$CH_4 + CO_2 + SO_4^{2-} \xrightarrow{R_{17}} 2HCO_3^- + H_2S \quad (17)$$

Adsorption reactions:

$$NH_4^+ \overset{K_N}{\rightleftharpoons} NH_4^+(ads) \quad (18)$$

$$\equiv S - H^0 + Mn^{2+} + HCO_3^- \overset{K_{Mn}}{\rightleftharpoons} \equiv S - Mn^+ + CO_2 + H_2O \quad (19)$$

$$\equiv S - H^0 + Fe^{2+} + HCO_3^- \overset{K_{Fe}}{\rightleftharpoons} \equiv S - Fe^+ + CO_2 + H_2O \quad (20)$$

Precipitation and dissolution reactions (non-redox):

$$x_{Mn}Mn^{2+} + (1 - x_{Mn})Ca^{2+} + 2HCO_3^- \overset{R_{21}, R_{-21}}{\rightleftharpoons} Ca_{1-x_{Mn}} \cdot Mn_{x_{Mn}} CO_3 + CO_2 + H_2O \quad (21)$$

$$x_{Fe}Fe^{2+} + (1 - x_{Fe})Ca^{2+} + 2HCO_3^- \overset{R_{22}, R_{-22}}{\rightleftharpoons} Ca_{1-x_{Fe}} \cdot Fe_{x_{Fe}} CO_3 + CO_2 + H_2O \quad (22)$$

$$Fe^{2+} + 2HCO_3^- + H_2S \overset{R_{23}, R_{-23}}{\rightleftharpoons} FeS + 2CO_2 + 2H_2O \quad (23)$$

Alkalinity conservation:

$$CO_3^{2-} + \delta CO_2 + (1 - \delta)H_2S + \delta H_2O \rightleftharpoons (1 + \delta)HCO_3^- + (1 - \delta)HS^-$$
$$0 \le \delta \le 1 \quad (24)$$

produces the reduced pore water species Mn^{2+}, Fe^{2+}, NH_4^+, H_2S, and CH_4, which may participate in secondary redox reactions, adsorb onto sediment particles, or (co)precipitate from solution (eqs 7-23). Many of the secondary redox reactions listed in table 2 may be catalyzed by microorganisms (Chapelle, 1993).

The model considers only the heterogeneous oxygenation of manganese(II) (eq 7) because of the exceedingly slow kinetics of the homogeneous reaction of Mn^{2+} with oxygen (Diem and Stumm, 1984). For iron, however, both homogeneous (eq 8) and heterogeneous (eq 9) oxygenation may proceed at measurable rates in natural aquatic environments (Davison and Seed, 1983; Wehrli, 1990). In addition, Fe^{2+} may be oxidized through reaction with manganese (hydr)oxides (eq 10) (Postma, 1985; De Vitre and others, 1988; Myers and Nealson, 1988; Burdige, Dhakar, and Nealson, 1992).

Net nitrification is represented by reaction (11) (Billen, 1982), pore water sulfide oxidation by reactions (12), (13), and (14) (Millero and others, 1987; Yao and Millero, 1993; Canfield, Raiswell, and Bottrell, 1992), and methane oxidation by reactions (16) and (17) (Berner, 1980; Devol and others, 1984; Iversen and Jørgensen, 1985). Note that pore water sulfide directly competes with organic carbon as reductant for the dissolution of iron and manganese (hydr)oxides in reactions (13) and (14). Reaction (15) accounts for the oxidative dissolution of authigenic iron sulfide mineral brought up into the aerobic zone via sediment mixing.

Ammonia adsorption (eq 18) is treated as a reversible, non-specific cation exchange reaction (Grim, 1968). The adsorption reactions of the metal cations Fe^{2+} and Mn^{2+} (eqs 19 and 20) are written as complexation reactions with hydrated surface sites (Davis and Kent, 1990; Dzombak and Morel, 1990). Adsorption sites for Fe^{2+} and Mn^{2+} in natural sediments are predominantly located on the surfaces of Fe/Mn (hydr)oxides and organic or biological particulates (Balistrieri, Brewer, and Murray, 1981; Lion, Altmann, and Leckie, 1982; Murray, Balistrieri, and Paul, 1984; Johnson, 1986; Sigg, 1987; Canfield, Thamdrup, and Hansen, 1993).

The profiles of dissolved Fe^{2+} and Mn^{2+} are often found to decrease with depth in the anaerobic portions of sediments. It is usually assumed that this reflects the precipitation of authigenic carbonate and sulfide mineral phases (eqs 21, 22, and 23). The model allows for both the precipitation and dissolution of the authigenic minerals. The coupling of the non-oxidative dissolution of iron sulfide (eq 23) to dissolved sulfide oxidation by manganese or iron (hydr)oxides (eqs 13 and 14) provides pathways for the oxidation of FeS in the absence of molecular oxygen. Aller and Rude (1988) have demonstrated experimentally that Mn oxides and possibly also Fe (hydr)oxides can oxidize solid phase sulfide in anoxic marine sediments (see also Canfield, Thamdrup, and Hansen, 1993).

The principal weak acids in natural pore waters are carbonic acid and, when sulfate reduction is important, hydrogen sulfide. In the model, we assume that the pore water pH is determined by the extent of dissociation of these two acids. Buffering is included in the model by writing reactions (1) to (23) in such a manner that any production or consumption of protons is balanced by rapid bicarbonate-carbonic acid interconversion. Consequently, the reaction stoichiometries describe the net production of pore water alkalinity by reactions (1) to (23). Local pH balance and alkalinity conservation is modeled by assuming internal equilibrium among the dissolved carbonate and sulfide species (reaction 24).

RATE LAWS AND EQUILIBRIUM CONDITIONS

Primary redox reactions.—Most kinetic descriptions of organic matter degradation used in early diagenetic models derive from the simple

first-order kinetic model (*G*-model) originally introduced by Berner (1964):

$$R_C = -\frac{d[CH_2O]}{dt} = k_C[CH_2O]_m \tag{25}$$

where R_C corresponds to the net rate of organic carbon oxidation, k_C is a first-order rate coefficient, $[CH_2O]$ is the concentration of organic carbon, and the subscript m refers to the metabolizable fraction of the organic carbon.

In the simplest possible approach, the rate coefficient k_C in eq (25) is assigned a single value, representative of the average reactivity of the sedimentary organic carbon over the depth range of interest (one-*G* model). More sophisticated *G*-type models which take into account the variability of organic matter reactivity with advancing degradation (for a recent review, see, Van Cappellen, Gaillard, and Rabouille, 1993) have been presented.

Several options for the total rate of organic carbon oxidation are available in the computer code we have developed. In one option, the user provides values for the deposition flux and rate coefficient of metabolizable organic carbon. The program then calculates the distributions of the carbon oxidation rate and the concentration of metabolizable organic carbon, using eq (25). In another option, the depth distribution of the total rate of organic carbon oxidation is imposed *a priori*. It is the latter option that is used in the simulations presented below. All options share one important feature: the total rate of organic carbon degradation is determined independently from the concentrations of species other than organic carbon. This is a characteristic inherent of the *G*-models for organic matter degradation (eq 25).

In the present model, the total rate of organic carbon oxidation is broken down into the contributions of the individual metabolic pathways represented by reactions (1) to (6). To this end, the model calculates the fractions f_i defined by

$$f_i = \frac{R_i}{R_C} \quad i = 1, \ldots, 6 \tag{26}$$

where R_i is the rate of carbon oxidation by the i-th pathway. Obviously, the rates R_i satisfy the following condition:

$$R_C = \sum_{i=1}^{6} R_i \tag{27}$$

To calculate fraction f_i, the model first determines whether the corresponding pathway is repressed by more energetic pathways. If not, the model checks whether the rate of the i-th pathway is limited or not by the availability of the external electron acceptor (note: this applies only to

the respiratory pathways, $i = 1$ to 5). The decision algorithm is based on a modified Monod formulation (Boudreau and Westrich, 1984; Gaillard and Rabouille, 1992) and assumes that for each of the five respiratory pathways there exists a critical or limiting concentration of the external oxidant. When the concentration of the oxidant exceeds the limiting value, the rate of the metabolic pathway is assumed to be independent of the concentration of the oxidant. In addition, the oxidation of organic carbon by energetically less powerful electron acceptors is inhibited. When the external oxidant concentration decreases below the limiting value, the rate is calculated by:

$$R_i = R_{\max} \frac{[EA]}{[EA]_{\lim}} \quad \text{for } [EA] < [EA]_{\lim} \tag{28}$$

where $[EA]$ is the concentration of the external oxidant, $[EA]_{\lim}$ is the limiting concentration, and $R_{\max}$ is the rate of oxidation when the supply of oxidant is not limiting ($[EA] \geq [EA]_{\lim}$).

The modified Monod kinetic formulation insures that with the exhaustion of the electron acceptor the corresponding organic carbon oxidation pathway comes to a halt. Furthermore, when $[EA] < [EA]_{\lim}$, the benthic heterotrophs begin utilizing oxidants with a lower intrinsic free energy yield. Use of the linear formulation of eq (28) increases computational efficiency and yields metabolic rate distributions that, for all practical purposes, are identical to those calculated with the full Monod law.

According to the computational procedure, methanogenesis (eq 6) is inhibited until the pore water sulfate concentration drops below its limiting value. When this happens, the contribution of methanogens to the overall degradation of organic carbon is calculated from:

$$f_6 = 1 - \sum_{i=1}^{5} f_i \tag{29}$$

In the model, the effects of oxidant limitation, metabolic inhibitors, and competition are all incorporated into the limiting oxidant concentrations, $[EA]_{\lim}$. Kinetic formulations for the inhibition of metabolic pathways and mechanisms for the competition between microbial populations have been presented in the literature (for a review, see, Van Cappellen, Gaillard, and Rabouille, 1993). Nonetheless, the implementation of oxidant limitation, inhibition, and competition as separate processes in the model would require a substantial number of additional parameters, most of which are poorly constrained. The use of a single $[EA]_{\lim}$ value per respiratory pathway offers the simplest way to deal with the complex physiological and ecological interactions that control the distribution of oxidant utilization in a sediment. It should be understood, however, that the $[EA]_{\lim}$ values represent apparent limiting concentrations, which may

deviate from true oxidant limiting concentrations, as measured for example in controlled microcosm experiments.

The calculation scheme developed for representing organic carbon breakdown and dissimilatory oxidant utilization results in smooth transitions between redox zones in the sediment column. The values of the limiting concentrations, $[EA]_{lim}$, control the extent of vertical overlap between the successive organic matter degradation pathways. The calculations require values for the limiting concentrations of the successive external electron acceptors, O_2, NO_3^-, Mn(IV), Fe(III), and SO_4^{2-}. Order-of-magnitude estimates of the apparent limiting concentrations of the dissolved oxidants in natural aquatic environments are available (Van Cappellen, Gaillard, and Rabouille, 1993; table 6). To our knowledge, no limiting concentrations have been reported for iron and manganese (hydr)oxide utilization. As shown later in this paper, modeling of the early diagenetic distributions of iron and manganese provides a way to constrain the limiting concentrations of Mn(IV) and Fe(III).

Secondary redox reactions.—In inorganic studies of redox reactions, rates are shown to correlate positively with the concentrations of both the oxidant and reductant participating in the reaction. As mentioned earlier, many of the secondary redox reactions in table 2 may in fact be microbially mediated. Although microbial involvement adds a new level of complexity, one may still expect the reaction kinetics to be limited by the availability of the terminal electron donor and the terminal electron acceptor. For example, Tebo and Emerson (1985) have shown that, at low reactant concentrations, the rate of microbial oxidation of manganese correlates positively with the concentrations of both Mn(II) and oxygen.

The available kinetic information on chemical and microbial redox processes imposes two fundamental requirements on the sediment rate model. First, the model should restrict the occurrence of a secondary redox reaction to that portion of the sediment where both the oxidant and the reductant have non-zero concentrations. Second, the rate laws should depend on the concentrations of the oxidant and the reductant. The most straightforward way to meet those requirements is to use bimolecular reaction rate laws for the secondary redox reactions (table 3, eqs 31-41).

For a number of abiotic redox reactions, experimental evidence directly supports the bimolecular rate laws used in the model. The rates of abiotic oxygenation of iron and manganese (eqs 7, 8, and 9), for example, have been shown to be proportional to the concentrations of oxygen and surface-bound or dissolved metal cations (Stumm and Lee, 1961; Morgan, Sung, and Stone, 1985; Wehrli, 1990; Stumm, 1992). Similarly, the inorganic oxidation kinetics of sulfide by oxygen and MnO_2 follow bimolecular rate laws (Millero and others, 1987; Yao and Millero, 1993). In those instances where detailed experimental information is unavailable, the bimolecular rate law represents the simplest, yet kinetically consistent, way to deal with the inorganic kinetics of redox reactions.

TABLE 3

Rate laws used in the model. The rate constants are assigned the following units:

$k_C, k_{-19}, k_{-20}, k_{-21}, k_{-22}, k_{-23}$: year^{-1}
k_7 to k_{17}, k_{19}, k_{20}: M^{-1} year^{-1}
k_{21}, k_{22}, k_{23}: mol g^{-1} year^{-1}

$$R_i = f_i k_C [CH_2O]_m \quad i = 1, \ldots, 6 \tag{30}$$
$$R_7 = k_7[\equiv S - Mn^+][O_2] \tag{31}$$
$$R_8 = k_8[Fe^{2+}][O_2] \tag{32}$$
$$R_9 = k_9[\equiv S - Fe^+][O_2] \tag{33}$$
$$R_{10} = k_{10}[MnO_2][Fe^{2+}] \tag{34}$$
$$R_{11} = k_{11}[NH_4^+][O_2] \tag{35}$$
$$R_{12} = k_{12} TS [O_2] \tag{36}$$
$$R_{13} = k_{13} TS [MnO_2] \qquad TS = [H_2S] + [HS^-] \tag{37}$$
$$R_{14} = k_{14} TS [Fe(OH)_3] \tag{38}$$
$$R_{15} = k_{15}[FeS][O_2] \tag{39}$$
$$R_{16} = k_{16}[CH_4][O_2] \tag{40}$$
$$R_{17} = k_{17}[CH_4][SO_4^{2-}] \tag{41}$$
$$R_{21} = k_{21}\delta_{21}\{\Omega_{Mn} - 1\} \tag{42}$$
$$R_{-21} = k_{-21}\delta_{-21}[MnCO_3](1 - \Omega_{Mn}) \tag{43}$$
$$R_{22} = k_{22}\delta_{22}(\Omega_{Fe} - 1) \tag{44}$$
$$R_{-22} = k_{-22}\delta_{-22}[FeCO_3](1 - \Omega_{Fe}) \tag{45}$$
$$R_{23} = k_{23}\delta_{23}(\Omega_{FeS} - 1) \tag{46}$$
$$R_{-23} = k_{-23}\delta_{-23}[FeS](1 - \Omega_{FeS}) \tag{47}$$

$$\Omega_{Mn} = \frac{[Mn^{2+}][CO_3^{2-}]}{x_{Mn} K'_{MnCO_3}} \qquad \begin{array}{l}\Omega_{Mn} > 1\text{: } \delta_{21} = 1, \delta_{-21} = 0 \\ \Omega_{Mn} \leq 1\text{: } \delta_{21} = 0, \delta_{-21} = 1\end{array}$$

$$\Omega_{Fe} = \frac{[Fe^{2+}][CO_3^{2-}]}{x_{Fe} K'_{FeCO_3}} \qquad \begin{array}{l}\Omega_{Fe} > 1\text{: } \delta_{22} = 1, \delta_{-22} = 0 \\ \Omega_{Fe} \leq 1\text{: } \delta_{22} = 0, \delta_{-22} = 1\end{array}$$

$$\Omega_{FeS} = \frac{[Fe^{2+}][HS^-]}{\{H^+\} K'_{FeS}} \qquad \begin{array}{l}\Omega_{FeS} > 1\text{: } \delta_{23} = 1, \delta_{-23} = 0 \\ \Omega_{FeS} \leq 1\text{: } \delta_{23} = 0, \delta_{-23} = 1\end{array}$$

[ ] = concentration; { } = activity; K' = conditional equilibrium constant.

In the case of microbially mediated secondary redox reactions, the use of bimolecular rate laws can be justified on theoretical grounds. The Monod law (or the Michaelis-Menten expression for enzymatically catalyzed kinetics) has been found to describe the dependence of microbial processes on limiting reactants in a wide variety of laboratory studies (Stanier, Adelberg, and Ingraham, 1980). When two limiting reactants are involved, the Monod rate law approaches a bimolecular rate expression when both reactants are present at low concentrations (Berner, 1980, p. 85). In natural aquatic environments, microbially catalyzed secondary redox reactions often operate in this limit case. The combination of relatively rapid kinetics and finite transport rates of the reactants results in fairly narrow reaction fronts where only low levels of the

reductant and oxidant can coexist. Under these conditions, the approximation of the bimolecular rate law should hold.

Adsorption reactions.—In the model, we assume that adsorption and desorption of ammonia, Fe^{2+}, and Mn^{2+} are fast relative to the characteristic transport time scales in sediments. Hence, equilibrium constants are used to describe the partitioning of the species between the pore solution and the surface sites.

Adsorption of ammonia is assumed to obey a simple linear equilibrium isotherm with a constant adsorption coefficient (Berner, 1980; Mackin and Aller, 1984). The relationship between the concentrations of adsorbed ammonia (in units of mass per unit mass total solids) and dissolved ammonia (in units of mass per unit volume pore solution) is given by:

$$[NH_4^+(ads)] = \frac{\phi K_N}{\rho(1-\phi)}[NH_4^+] \tag{48}$$

where K_N is the dimensionless adsorption coefficient, ϕ the porosity, and ρ the average solid density. A constant value of K_N implies that the concentration and nature of the adsorption sites for ammonia do not vary greatly within the sediment. This will be the case when ammonia adsorption is mostly restricted to the exchangeable positions in a detrital clay fraction of fairly constant composition and concentration (Grim, 1968).

Adsorption of iron and manganese is more complicated because the concentrations of the major adsorbents of Fe^{2+} and Mn^{2+} may vary widely in a sediment. This is true particularly for the (hydr)oxides of Fe and Mn which tend to be concentrated in the top sediment. Canfield, Thamdrup, and Hansen (1993) have shown that the adsorption capacity for Mn^{2+} in a marine sediment off the coast of Denmark decreases by over an order of magnitude between the oxidized surface layer and the deeper anoxic sediment. The decrease in adsorption capacity at this site correlates with the decrease in the manganese (hydr)oxide content of the sediment.

Recognizing the importance of Fe/Mn (hydr)oxides as metal cation adsorbents, the total number of surface donor groups that can potentially form coordination complexes with Fe^{2+} and Mn^{2+} is expressed as

$$S_T = S_b + S_{Fe(OH)_3} + S_{MnO_2} \tag{49}$$

where S_T is the total concentration of surface sites, while $S_{Fe(OH)_3}$ and S_{MnO_2} are the concentrations of surface groups associated with reactive iron and manganese (hydr)oxides, respectively. For simplicity, the concentration of surface sites on mineral and organic substrates other than reactive iron and manganese (hydr)oxides (S_b) is kept constant. The surface site concentrations $S_{Fe(OH)_3}$ and S_{MnO_2} can be derived from the concentrations of the reactive iron and manganese (hydr)oxides and the surface site densities of the solids. According to Balistrieri and Murray (1982) the number of surface hydroxyl groups is approx 11 mmoles g^{-1}

on amorphous iron hydroxide and 27 mmoles g^{-1} on poorly crystalline MnO_2.

The concentrations of adsorbed Fe^{2+} and Mn^{2+} are calculated using the following equilibrium expressions:

$$[\equiv S - Fe^{+}] = K^{s*}_{Fe}[Fe^{2+}]S_f \tag{50}$$

and

$$[\equiv S - Mn^{+}] = K^{s*}_{Mn}[Mn^{2+}]S_f \tag{51}$$

where K^{s*}_{Fe} and K^{s*}_{Mn} are apparent stability constants of the surface complexes and S_f is the concentration of unoccupied (free) surface sites. In the case of a single adsorbent, the apparent or conditional stability constants depend on pH, ionic strength, and the net surface charge (Schindler and Stumm, 1987; Davis and Kent, 1990; Stumm, 1992; Van Cappellen and others, 1993). In a natural sediment, the apparent constants also reflect the relative abundances and binding affinities of the various particulate surfaces. In practice, it is fairly difficult to predict theoretical values for K^{s*}_{Fe} and K^{s*}_{Mn} in natural systems (Sigg, 1987). Therefore, we treat the apparent surface complexation constants as adjustable parameters in the model.

In order to apply eqs (50) and (51), the number of unoccupied or free surface sites must be known. The latter is obtained from the site balance condition:

$$S_f = S_T - [\equiv S - Fe^{+}] - [\equiv S - Mn^{+}] - \sum [\equiv S - X] \tag{52}$$

where $\equiv S - X$ represents surface sites complexed by ions other than protons, Fe^{2+}, or Mn^{2+}. In a system where the major ion composition of the solution does not change it is convenient to rewrite eq (52) as,

$$S_f = \frac{1}{1 + \gamma_s}\{S_T - [\equiv S - Fe^{+}] - [\equiv S - Mn^{+}]\} \tag{53}$$

where γ_s is related to the relative abundance of $\equiv S - X$ sites. If we assume that surface hydroxyls on (hydr)oxide minerals are representative of surface sites in natural sediments, then we can use (hydr)oxide surface speciation calculations to constrain the range of values of γ_s. Balistrieri and Murray (1982) have calculated that in seawater (pH = 8) 10 to 15 percent of the available adsorption sites on goethite and hydrous manganese dioxide are complexed by ions other than H^+, mostly Mg^{2+}. Thus, in marine sediments the values of γ_s should fall in the range 0.11 to 0.18. Lower values of γ_s are expected in freshwater sediments.

Non-redox precipitation and dissolution.—Mineral precipitation or dissolution is driven by the degree of saturation of the pore waters with respect to the mineral phase. The dependence on saturation state is included explicitly in the rate laws of precipitation and dissolution of authigenic

iron and manganese minerals (eqs 42-47). The apparent rate constants appearing in the rate laws incorporate the catalyzing or inhibiting actions of solution constituents. They also include the effect of the amount of reactive mineral surface area. The latter is probably one of the most difficult parameters to constrain in natural aquatic systems (Steefel and Van Cappellen, 1990).

In the model, the rate laws describing the precipitation of authigenic carbonate and sulfide phases are independent of the concentrations of the respective mineral phases (see eqs 42, 44, and 46). Strictly speaking, this cannot be true because the availability of reactive surface area varies with the concentration of a solid. It does, however, lead to a rate law where the precipitation of a mineral is never limited by its own surface area. The kinetic formulation, therefore, incorporates the possibility of nucleating a mineral in a sediment layer that initially does not contain that mineral. This is, obviously, a requirement for the formation of authigenic minerals. The rates of dissolution of the authigenic minerals are assumed to be proportional to the concentrations of the corresponding solid phases (eqs 43, 45, and 47). Accordingly, dissolution stops when there is no more mineral left.

Alkalinity conservation.—The model assumes that pore water pH is buffered by the dissolved carbonate and sulfide species. It is, therefore, useful to cast the acid-base chemistry of the pore waters in terms of the following conservative parameters:

$$TC = [CO_2^*] + [HCO_3^-] + [CO_3^{2-}] \tag{54}$$

$$TS = [H_2S] + [HS^-] \tag{55}$$

$$ALK = [HCO_3^-] + 2[CO_3^{2-}] + [HS^-] \tag{56}$$

$$ALK_c = [HCO_3^-] + 2[CO_3^{2-}] \tag{57}$$

where TC stands for total dissolved CO_2 (CO_2^* is the sum of hydrated and unhydrated dissolved carbonic acid), TS for total dissolved sulfide, ALK for total alkalinity, and ALK_c for carbonate alkalinity.

The principal approximation made in the pore water acid-base model is the simplified representation of the total alkalinity (eq 56), which neglects the contributions of minor inorganic bases ($B(OH)_4^-$, NH_3, HPO_4^{2-}, $H_3SiO_4^-$) and dissolved organic anions (Gaillard, Pauwels, and Michard, 1989; Cantrell, Serkiz, and Perdue, 1990). Under certain circumstances, these contributions could conceivably be significant, for example in highly organic-rich sediments. It should be noted that the inclusion of additional pore water buffering components in future versions of the model will be possible without modification of the general computational approach.

The relative distribution of species in the dissolved carbonate-sulfide system is controlled by the following mixed acid dissociation constants:

$$K'_{1C} = \frac{\{H^+\}[HCO_3^-]}{[CO_2^*]}, \tag{58}$$

$$K'_{2C} = \frac{\{H^+\}[CO_3^{2-}]}{[HCO_3^-]}, \tag{59}$$

and

$$K'_{1S} = \frac{\{H^+\}[HS^-]}{[H_2S]} \tag{60}$$

where $\{H^+\}$ is the proton activity (table 4). The conditional acidity constants are corrected for temperature and salinity in the model (Van Cappellen and Wang, 1995).

As discussed below, the model solves the conservation equations of total dissolved CO_2, total dissolved sulfide, and total alkalinity. The three conservation equations are coupled to the assumption of internal equilibrium in the dissolved carbonate-sulfide system. This is equivalent to assuming that the homogeneous acid-base reactions are fast with respect to the characteristic transport time scales. Through iteration it is then

TABLE 4

Equilibrium distribution coefficients appearing in the continuity equations of total dissolved carbon dioxide (TC), total dissolved sulfide (TS), and total alkalinity (ALK)

$$\alpha_{0C} = \frac{[CO_2^*]}{TC} = \left(1 + \frac{K'_{1C}}{\{H^+\}} + \frac{K'_{1C}K'_{2C}}{\{H^+\}^2}\right)^{-1} \tag{61}$$

$$\alpha_{1C} = \frac{[HCO_3^-]}{TC} = \left(\frac{\{H^+\}}{K'_{1C}} + 1 + \frac{K'_{2C}}{\{H^+\}}\right)^{-1} \tag{62}$$

$$\alpha_{2C} = \frac{[CO_3^{2-}]}{TC} = \left(\frac{\{H^+\}^2}{K'_{1C}K'_{2C}} + \frac{\{H^+\}}{K'_{2C}} + 1\right)^{-1} \tag{63}$$

$$\alpha_{0S} = \frac{[H_2S]}{TS} = \left(1 + \frac{K'_{1S}}{\{H^+\}}\right)^{-1} \tag{64}$$

$$\alpha_{12S} = \frac{[HS^-]}{TS} = \left(1 + \frac{\{H^+\}}{K'_{1S}}\right)^{-1} \tag{65}$$

$$\beta_{1C} = \frac{[HCO_3^-]}{ALK} = \frac{\alpha_{1C}TC}{(\alpha_{1C} + 2\alpha_{2C})TC + \alpha_{1S}TS} \tag{66}$$

$$\beta_{2C} = \frac{[CO_3^{2-}]}{ALK} = \frac{\alpha_{2C}TC}{(\alpha_{1C} + 2\alpha_{2C})TC + \alpha_{1S}TS} \tag{67}$$

$$\beta_{1S} = \frac{[HS^-]}{ALK} = \frac{\alpha_{1S}TS}{(\alpha_{1C} + 2\alpha_{2C})TC + \alpha_{1S}TS} \tag{68}$$

possible to calculate the distributions of TC, TS, ALK, ALK_c, and pH. Local acid-base equilibrium leads to the following relationship for pore water pH:

$$\{H^+\} = \frac{K'_{1C}}{2ALK_c} \cdot \left((TC - ALK_c) + \left[(TC - ALK_c)^2 - 4ALK_c \frac{K'_{2C}}{K'_{1C}} (ALK_c - 2TC) \right]^{1/2} \right) \quad (69)$$

TRANSPORT FLUXES

The transport processes included in the model are sediment advection, particle mixing by macrofauna (bioturbation), molecular pore water diffusion, and pore water irrigation. The fluxes are described using standard expressions that have been presented in the literature.

Sediment reworking by macrobenthos is modeled as a random mixing process quantified by a biodiffusion coefficient, D_{mix} (Berner, 1980). Particle mixing affects the transport of solid, interfacial and dissolved species. The diffusional coefficients appearing in the conservation equations are:

$$\begin{aligned} D &= D_{sed} + D_{mix} && \text{for a solute} \\ D &= D_{mix} && \text{for a solid or interfacial species} \end{aligned} \quad (70)$$

where D_{sed} is the molecular diffusion coefficient corrected for temperature, sediment tortuosity, and pore water viscosity. Numerical values of relevant molecular diffusion coefficients have been tabulated by Li and Gregory (1974), Berner (1980), Tromp, Van Cappellen, and Key (1995), and Van Cappellen and Wang (1995).

A number of different models have been presented to describe the enhancement of solute exchanges by irrigation. Here, we use a simple non-local model:

$$S(x) = \alpha_x (C_0 - C_x) \quad (71)$$

where C_0 and C_x are the concentrations of the solute in the overlying water and at depth x below the water-sediment interface, α_x is the solute exchange coefficient at depth x, and $S(x)$ is the irrigation source strength in units of solute concentration per unit time (Emerson, Jahnke, and Heggie, 1984; Boudreau, 1984).

In the model, both the biodiffusion coefficient, D_{mix}, and the irrigation coefficient, α_x, are allowed to vary with depth in the sediment. Usually, bioturbation and irrigation are most intense in the upper few centimeters of the sediment, although they often persist to depths of 20 to 30 cm or more (Martin and Sayles, 1987; McNichol, Lee, and Druffel, 1988; Gerino and Stora, 1991).

CONSERVATION EQUATIONS

With the exception of the carbonate species, sulfide species, and protons, all solutes in table 1 are represented by the following transport-reaction equation:

$$\partial_t C = \partial_x(D\partial_x C) - \partial_x(\omega C) + \alpha_x(C_0 - C) + R \tag{72}$$

where C is the concentration of the solute (mass per unit volume pore water), D is the diffusional coefficient (eq 70), α_x is the irrigation coefficient, C_0 is the bottom water concentration, R is the net rate of production of the solute, and ∂_t and ∂_x are the partial derivatives with respect to time and depth, respectively.

Inclusion of equilibrium adsorption modifies the conservation equations of dissolved ammonia, dissolved Mn^{2+} and dissolved Fe^{2+} to:

$$\partial_t[(1 + K)C] = \partial_x(D_{mix}\partial_x[(1 + K)C]) + \partial_x(D_{sed}\partial_x C) - \partial_x(\omega[(1 + K)C]) + \alpha_x(C_0 - C) + R' + FR_s' \tag{73}$$

where R' and R_s' are the net rates of production of the dissolved and adsorbed species by all non-equilibrium reactions. The conversion factor F is defined as

$$F = \frac{\rho(1 - \phi)}{\phi} \tag{74}$$

(Berner, 1980). For ammonia, the adsorption coefficient K appearing in eq (73) is simply the non-dimensionless adsorption constant K_N defined in eq (48). For Mn^{2+} and Fe^{2+}, the coefficient K is given by

$$K_{(Mn,Fe)} = FK^{s*}_{Mn,Fe}S_f \tag{75}$$

The concentration of free surface sites S_f is obtained by combining the calculated concentrations of adsorbed Fe(II) and Mn(II) with the surface site balance (eq 53). The distributions of the interfacial species are calculated directly from the pore water concentrations of ammonia, Mn^{2+} and Fe^{2+}, using eqs (48), (50), and (51).

The conservation equations describing the concentration distributions of the solid species are:

$$\partial_t C = \partial_x(D_{mix}\partial_x C) - \partial_x(\omega C) + R \tag{76}$$

where C is now the particulate concentration (in units of mass per unit mass dry sediment. For simplicity, the conservation equations derived above assume constant values of porosity, ϕ, and average solid density, ρ. These restrictions, however, can easily be relaxed in the numerical model.

In general, the net rate R (or R') appearing in the continuity equation of a given species depends on the concentrations of other species, thus coupling the species distributions to one another. The

exception is organic carbon whose rate term depends only on the concentration of organic carbon itself. The expressions for the net rates R or R' can be found in table 5.

TABLE 5

Rate expressions in the transport-reaction equations. F is the conversion factor defined by eq (74) in the text

$$R_{O_2} = F\left(-\frac{x+2y}{x}R_1 - \frac{R_7}{2} - \frac{R_9}{4} - 2R_{15}\right) - \left(\frac{R_8}{4} + 2R_{11} + 2R_{12} + 2R_{16}\right) \tag{77}$$

$$R_{NO_3^-} = F\left(\frac{y}{x}R_1 - \frac{4x+3y}{5x}R_2\right) + R_{11} \tag{78}$$

$$R'_{Mn^{2+}} = F(2R_3 + R_{10} + R_{13} - x_{Mn}R_{21} + x_{Mn}R_{-21}) \tag{79}$$

$$R'_{Fe^{2+}} = F(4R_4 - 2R_{10} + 2R_{14} + R_{15} - x_{Fe}R_{22} + x_{Fe}R_{-22}) - R_8 \tag{80}$$

$$R_{SO_4^{2-}} = F\left(-\frac{R_5}{2} + R_{15}\right) + R_{12} - R_{17} \tag{81}$$

$$R'_{NH_4^+} = F\frac{y}{x}(R_3 + R_4 + R_5 + R_6) - R_{11} \tag{82}$$

$$R_{CH_4} = \frac{F}{2}R_6 - R_{16} - R_{17} \tag{83}$$

$$R'_{\equiv S-Mn^+} = -R_7 \tag{84}$$

$$R'_{\equiv S-Fe^+} = -R_9 \tag{85}$$

$$R'_{NH_4^+(ads)} = 0 \tag{86}$$

$$R_{CH_2O} = -(R_1 + R_2 + R_3 + R_4 + R_5 + R_6) \tag{87}$$

$$R_{MnO_2} = -2R_3 + R_7 - R_{10} - R_{13} \tag{88}$$

$$R_{Fe(OH)_3} = -4R_4 + \frac{R_8}{F} + R_9 + 2R_{10} - 2R_{14} \tag{89}$$

$$R_{MnCO_3} = x_{Mn}(R_{21} - R_{-21}) \tag{90}$$

$$R_{FeCO_3} = x_{Fe}(R_{22} - R_{-22}) \tag{91}$$

$$R_{FeS} = -R_{15} + R_{23} - R_{-23} \tag{92}$$

$$R_{TC} = F\left(R_1 + R_2 + R_3 + R_4 + R_5 + \frac{R_6}{2} - R_{21} + R_{-21} - R_{22} + R_{-22}\right) + R_{16} + R_{17} \tag{93}$$

$$R_{TS} = F\left(\frac{R_5}{2} - R_{13} - R_{14} - R_{23} + R_{-23}\right) - R_{12} + R_{17} \tag{94}$$

$$\begin{aligned} R_{ALK} = F\Bigg(&-\frac{y+2z}{x}R_1 + \frac{4x+3y-10z}{5x}R_2 + \frac{4x+y-2z}{x}R_3 + \frac{8x+y-2z}{x}R_4 \\ &+ \frac{x+y-2z}{x}R_5 + \frac{y-2z}{x}R_6 - R_7 - R_9 - 2R_{10} + 2R_{13} + 4R_{14} - R_{19} - R_{20} \\ &- 2R_{21} + 2R_{-21} - 2R_{22} + 2R_{22} - 2R_{23} + 2R_{-23}\Bigg) - 2R_8 - 2R_{11} - 2R_{12} + 2R_{17} \end{aligned} \tag{95}$$

A set of transport-reaction equations is also required to account for the early diagenesis of the dissolved carbonate-sulfide system. The equations are obtained by coupling the irreversible productions of total dissolved carbonate, total dissolved sulfide, and total alkalinity to internal equilibrium among the dissolved carbonate and sulfide species. This leads to the following conservation equations for *TC*, *TS*, and *ALK*:

$$\partial_t TC = \partial_x\{D_{CO_2}\partial_x(\alpha_{0C}TC) + D_{HCO_3^-}\partial_x(\alpha_{1C}TC) + D_{CO_3^{2-}}\partial_x(\alpha_{2C}TC)\} - \partial_x(\omega TC) + \alpha_x(TC_0 - TC) + R_{TC} \quad (96)$$

$$\partial_t TS = \partial_x\{D_{H_2S}\partial_x(\alpha_{0S}TS) + D_{HS^-}\partial_x(\alpha_{1S}TS)\} - \partial_x(\omega TS) + \alpha_x(TS_0 - TS) + R_{TS} \quad (97)$$

$$\partial_t ALK = \partial_x\{D_{HCO_3^-}\partial_x(\beta_{1C}ALK) + 2\partial_x D_{CO_3^{2-}}\partial_x(\beta_{2C}ALK) + D_{HS^-}\partial_x(\beta_{1S}ALK)\} - \partial_x(\omega ALK) + \alpha_x(ALK_0 - ALK) + R_{ALK} \quad (98)$$

where the α and β coefficients are obtained from the equilibrium distributions in the dissolved carbonate-sulfide system (table 4). The rate terms in the conservation equations are given in table 5 (eqs 93, 94, and 95).

Expressions for the rates appearing in the production of total pore water alkalinity (eq 95) can be found in table 3, except for the rates R_{19} and R_{20} which are associated with the equilibrium adsorption reactions of Mn^{2+} and Fe^{2+}. The surface complexation reactions of the metals (reactions 19 and 20) consume alkalinity and therefore their effects must be incorporated in the conservation equation of *ALK*. This is done by calculating the net rates of adsorption of Mn^{2+} and Fe^{2+} from the mass balance conditions:

$$R_{19}(x, t) = \partial_t[\equiv S - Mn^+] - \partial_x(D_{mix}\partial_x[\equiv S - Mn^+]) + \partial_x(\omega[\equiv S - Mn^+]) - R'_{\equiv S-Mn^+} \quad (99)$$

and

$$R_{20}(x, t) = \partial_t[\equiv S - Fe^+] - \partial_x(D_{mix}\partial_x[\equiv S - Fe^+]) + \partial_x(\omega[\equiv S - Fe^+]) - R'_{\equiv S-Fe^+} \quad (100)$$

where the differential quantities on the right-hand sides of eqs (99) and (100) are evaluated numerically at the given depth (x) and time (t) of interest.

BOUNDARY CONDITIONS

The upper boundary condition ($x = 0$) for a pore water constituent is its bottom water concentration. For a solid-bound species, the deposi-

tion flux from the water column is imposed. The flux continuity condition for a solid or interfacial species at the water-sediment interface is then:

$$\frac{J_0}{\rho(1-\phi)} = \{-D_{mix}\partial_x C + \omega C\}\,|_{x=0} \tag{101}$$

where J_0 is the deposition flux (in mass per unit sediment surface area per unit time). The right hand side of eq (101) is evaluated for the parameter values, concentration, and concentration gradient at the water-sediment interface.

As lower boundary conditions we assume that all concentration gradients vanish at sufficiently great depth in the sediment. Both upper and lower boundary conditions are easily included in a numerical finite-difference scheme (see next section). It is important to note that the model requires no intermediate sets of boundary conditions. Hence, the development of a vertical zonation of chemical conditions is due solely to the coupled dynamics of reaction and transport processes within the surface sediment.

NUMERICAL SOLUTION

The mass conservation eqs (72), (73), (76), (96), (97), and (98) are solved numerically with a finite difference method. The sediment column ($0 \le x \le L$) is divided into n intervals of length Δx, and the equations are then discretized with respect to depth and time. For instance, discretization of eq (72) at spatial node l and time step m gives,

$$\frac{C_l^m - C_l^{m-1}}{\Delta t} = \frac{1}{(\Delta x)^2}\left[D_{l+1/2}^m C_{l+1}^m - (D_{l+1/2}^m + D_{l-1/2}^m)C_l^m + D_{l-1/2}^m C_{l-1}^m\right]$$

$$- \frac{1}{\Delta x}\left[\omega_l^m C_l^m - \omega_{l-1}^m C_{l-1}^m\right] + \alpha_l^m(C_1^m - C_l^m) + R_l^m \tag{102}$$

where

$$C_l^m = C((l-1)\Delta x, m\Delta t), \tag{103}$$

$$D_{l+1/2}^m = \frac{1}{2}\{D_{l+1}^m + D_l^m\} \tag{104}$$

The major complication in solving the set of finite difference equations arises from the presence of the nonlinear reaction rate terms which couple the conservation equations. This requires an iterative method of solution (see also, Steefel and Lasaga, 1994). In our algorithm, the

concentrations of the species at the hth iteration step are calculated from (using eq 72 as an example):

$$\frac{C_l^{m,h} - C_l^{m-1,h}}{\Delta t} = \frac{1}{(\Delta x)^2}[D^m_{l+1/2}C^{m,h}_{l+1} - (D^m_{l+1/2} + D^m_{l-1/2})C^{m,h}_l + D^m_{l-1/2}C^{m,h}_{l-1}]$$
$$- \frac{1}{\Delta x}[\omega^m_l C^{m,h}_l - \omega^m_{l-1}C^{m,h}_{l-1}] + \alpha^m_l(C^m_1 - C^{m,h}_l) + R^{m,h-1}_l$$
$$+ \frac{\partial R^{m,h-1}_l}{\partial C}(C^{m,h}_l - C^{m,h-1}_l) + H(C^{m,h}_l - C^{m,h-1}_l) \quad (105)$$

with $C_l^{m,0} = C_l^{m-1}$. The last term on the right-hand side of eq (105) is added to speed up the convergence of the iteration; H is an adjustable numerical constant.

With proper boundary conditions, the linearized finite difference equations (eq 105) are solved, species by species, using the Thomas algorithm (Huyakorn and Pinder, 1983). Iteration proceeds until convergence, defined as

$$\frac{\underset{l}{Max}\,|C_l^{m,h} - C_l^{m,h-1}|}{\underset{l}{Max}\,|C_l^{m,h}|} < \varepsilon \quad \text{for all independent species} \quad (106)$$

where ε, the error tolerance, is typically set at 10^{-6}. Once the system of equations has converged, the calculation moves on to the next time step $m + 1$. The same method of solution is used when solving the conservation equations at steady state. In that case, however, the left-hand side of eq (105) is made equal to zero. Interested researchers can obtain a copy of the software of the steady state version of the model (STEADYSED1) by contacting the authors.

After completion of an iteration, mass balance conditions for the various elements can be checked: local fluxes are calculated at the boundaries, and quadrature of the distributions of rates and irrigation source strength are performed between the boundaries. In all cases we have tested, mass imbalances were well below 1 percent. Examples of the excellent mass balances for iron and manganese are illustrated in figure 12.

APPLICATION

The authors have used an earlier, simpler version of the model to simulate the distribution, cycling, and burial of iron and manganese in a set of hypothetical marine and freshwater surface sediments (Van Cappellen and Wang, 1995). The relative contributions of dissimilatory and chemical pathways for the reductive dissolution of iron and manganese (hydr)oxides were found to vary substantially from one depositional setting to another. For example, the model predicts that iron (hydr)oxide reduction in coastal-estuarine sediments is, for the most part, directly coupled to the oxidation of organic carbon (eq 4). In slower accumulating

shelf sediments, however, chemical reduction by sulfide dominates (eq 14). Manganese (hydr)oxides, on the other hand, were found to be mostly reduced by pore water Fe^{2+} in both coastal and shelf sediments (eq 10). The simulations also showed that the pore water pH and alkalinity profiles are very sensitive to the relative importance and spatial distributions of the various biogeochemical reactions.

The results of our earlier study showed that the model realistically reproduces some of the essential features of the sedimentary biogeochemical dynamics of oxygen, carbon, nitrogen, sulfur, iron, and manganese. However, the model predictions were not directly tested using existing field data. In this paper, we compare model output with data collected by Canfield and coworkers in a Danish coastal sediment (Canfield, Thamdrup, and Hansen, 1993; Canfield and others, 1993). These researchers provide a remarkably complete set of pore water and solid sediment analyses. Furthermore, they performed sediment incubation experiments that allowed the direct measurement of the rates of production (or consumption) of some of the critical reactive species as a function of depth.

Site description.—Canfield and his coworkers have described three sites in the eastern Skagerrak, between Denmark and Norway. Here, we consider one of the sites (S_4). The two other sites (S_6 and S_9) are the subject of a forthcoming publication (Wang and Van Cappellen, unpublished). Site S_4 is the shallowest of the three sites (190 m water depth). The sedimentation rates in the area are in the range 0.1 to 0.2 cm yr^{-1}. For site S_4 we use the higher value of 0.2 cm yr^{-1} based on the generally observed inverse correlation between sedimentation rate and water depth in the oceans (Tromp, Van Cappellen, and Key, 1995). The depth-integrated carbon oxidation rate reported by Canfield and coworkers for site S_4 is 5.8 moles C m^{-2} yr^{-1}. Oxygen penetrates to a depth of approx 0.7 cm below the water-sediment surface interface. Pore water and solid phase analyses, as well as sediment incubation experiments, show that manganese and iron (hydr)oxides are reduced mostly within the upper 2 to 4 cm of sediment. Both the evidence reported in the studies by Canfield and coworkers and the modeling work discussed below indicate that bioturbation and bioirrigation significantly affect the chemical conditions in the sediment. In the absence of time series information, the simulations assume steady state conditions at the site.

Parameter estimation.—The values of the various model parameters used in the simulations have been compiled in table 6. Three different classes of parameters are distinguished: independent, constrained, and fitted parameters. Values of the independent parameters are determined *a priori*, based on experimental or field information extraneous to the actual data that is being simulated. Parameters for which it is possible to bracket the possible range of values are referred to as constrained parameters. For some parameters, no independent information was found to estimate or otherwise constrain the parameter value. These are the fitted parameters whose values were obtained entirely from matching

TABLE 6

Parameter values used in the model simulations. (I) Independent, (C) constrained, and (M) model-derived parameter. See text for the definitions of the three types of parameters

Parameter	Value	Range	Type	Source
sedimentation rate	0.2 cm yr^{-1}		I	1, 2
temperature	5°C		I	1, 2
$F = \rho[(1 - \phi)/\phi]$	0.6 g cm^{-3}	0.2–1.0	C	3
D_{mix}	20 cm^2 yr^{-1}	4–40	C	4, 5
x_{mix}	25 cm	5–30	C	3
α_0 (eq 108)	200 yr^{-1}	2–300	C	6, 7
α_1 (eq 108)	0.28 cm^{-1}	0.02–1.0	C	7
$[O_2]_0$	231 μM		I	2
$[NO_3^-]_0$	1.5 μM	0–20	C	2, 8
$[SO_4^{2-}]_0$	28 mM		I	5
$[Mn^{2+}]_0$	2 μM		I	1
$[Fe^{2+}]_0$	0		I	1
$[NH_4^+]_0$	22 μM	0.1–25	C	1, 8
TS_0	0		I	9
ALK_0	2.5 meq dm^{-3}		I	10
pH_0	7.9		I	10
R_0 (eq 107)	135 μmol cm^{-3} yr^{-1}		I	see text
β (eq 107)	0.208 cm^{-1}		I	see text
C:N	8.8	3.3–11	C	1, 8
C:P	106	68–150	C	11
J_{Fe} (eq 101)	75 μmol cm^{-2} yr^{-1}		M	
J_{Mn} (eq 101)	40 μmol cm^{-2} yr^{-1}		M	
$[O_2]_{lim}$	20 μM	1–30	C	12
$[NO_3^-]_{lim}$	5 μM	4–80	C	12
$[SO_4^{2-}]_{lim}$	1600 μM	1600	C	12
$[MnO_2]_{lim}$	16 μmol g^{-1}		M	
$[Fe(OH)_3]_{lim}$	100 μmol g^{-1}		M	
K_N (eq 48)	1.4	0.8–1.7	C	13
K_{Mn}^{S*} (eq 51)	$10^{3.5}$	$10^{2.1}$–$10^{5.5}$	C	14
K_{Fe}^{S*} (eq 50)	$10^{3.7}$	$10^{2.4}$–$10^{5.8}$	C	14
S_b (eq 49)	30 μmol g^{-1}		M	
K'_{MnCO_3}	$10^{-8.5}$		I	15, 16
K'_{FeCO_3}	$10^{-8.4}$		I	16, 17
K'_{FeS}	$10^{-2.2}$		I	16, 18
x_{Mn} (eq 21)	1	0–1	C	
x_{Fe} (eq 22)	1	0–1	C	
k_7	5×10^6 M^{-1} yr^{-1}	8×10^5–2×10^7	C	19
k_8	1.4×10^8 M^{-1} yr^{-1}		I	20
k_9	5×10^7 M^{-1} yr^{-1}	$\leq 10^8$	C	19
k_{10}	3×10^6 M^{-1} yr^{-1}	$\leq 10^9$	C	21
k_{11}	5×10^6 M^{-1} yr^{-1}	$\approx 10^7$	C	22
k_{12}	1.6×10^5 M^{-1} yr^{-1}	$\geq 1.6 \times 10^5$	C	23
k_{13}	2×10^4 M^{-1} yr^{-1}	$\leq 10^8$	C	24
k_{14}	8×10^3 M^{-1} yr^{-1}	$\leq 10^5$	C	25
k_{15}	3×10^5 M^{-1} yr^{-1}		M	

TABLE 6
(continued)

Parameter	Value	Range	Type	Source
k_{16}	$10^{10}\ M^{-1}\ yr^{-1}$		M	
k_{17}	$10^{4}\ M^{-1}\ yr^{-1}$	$\approx 10^{4}$	C	26
k_{21}	$1 \times 10^{-4}\ mol\ g^{-1}\ yr^{-1}$	$< 10^{-2}$	C	17, 27
k_{-21}	$2.5 \times 10^{-1}\ yr^{-1}$	10^{-2}–10^{3}	C	17, 27
k_{22}	$4.5 \times 10^{-4}\ mol\ g^{-1}\ yr^{-1}$	$< 10^{-2}$	C	17, 27
k_{-22}	$2.5 \times 10^{-1}\ yr^{-1}$	$\geq 10^{-2}$	C	17, 27
k_{23}	$1.5 \times 10^{-5}\ mol\ g^{-1}\ yr^{-1}$		M	
k_{-23}	$1 \times 10^{-3}\ yr^{-1}$		M	

1. Canfield, Thamdrup, and Hansen (1993); 2. Canfield and others (1993); 3. Tromp (personal communication); 4. Van Cappellen, Gaillard, and Rabouille (1993); 5. Tromp, Van Cappellen, and Key (1995); 6. Emerson, Jahnke, and Heggie (1984); 7. Martin and Banta (1992); 8. Enoksson, Sörensson, and Granéli (1990); 9. Thamdrup and others (1994); 10. Canfield (personal communication); 11. Van Cappellen and Berner (1988); 12. Van Cappellen and Wang (1995); 13. Mackin and Aller (1984); 14. Smith and Jenne (1991); 15. Johnson (1982); 16. Millero and Schreiber (1982); 17. Wersin (1990); 18. Davison (1991); 19. Wehrli (1990); 20. Millero, Sotolongo, and Izaguirre (1987); 21. Myers and Nealson (1988); 22. Billen (1982); 23. Millero and others (1987); 24. Yao and Millero (1993); 25. Pyzik and Sommer (1981); 26. Iversen and Jørgensen (1985); 27. Wollast (1990).

calculated and observed profiles of species concentrations or reaction rates.

A broad literature survey enabled us to reduce the number of fitted parameters to a minimum (table 6). No information was found to constrain the limiting oxidant concentrations of dissimilatory iron and manganese reduction, as well as four of the reaction rate constants (k_{15}, k_{16}, k_{23}, k_{-23}). Of the latter, the rate constant of aerobic methane oxidation (k_{16}) is inconsequential for the present simulation, because methane production is negligible at site S_4.

Although most model parameters can somehow be estimated or constrained independently, it must be recognized that they often have substantial uncertainties associated with them. For many reaction rates constants, for instance, it is only possible to specify a limit value, rather than an actual range of values (table 6). This reflects the complexity of biotic and abiotic catalysis and inhibition that characterizes biogeochemical reactions in natural aquatic environments.

At first glance, the great number of model parameters involved may seem to imply a large degree of freedom when fitting the data. One could therefore object that an agreement between model calculations and data may say little about the validity of the model. Consider that we are fitting the observed distribution of a single species. An error in, say, the formulation or parameterization of one of the transport fluxes of that species may be carried over in the value of an adjustable reaction rate constant controlling the production or consumption of that species (an example involving organic carbon distributions is given in Van Cappellen, Gaillard, and Rabouille, 1993). The situation changes, however,

when we consider an increasing number of reactive species that are coupled to one another via reaction and transport.

In a coupled, multicomponent model a single set of parameters must account for the distributions of all the species. This greatly limits the latitude we have in adjusting parameter values. For instance, the irrigation coefficient (α_x) appears in the continuity equations of all the independent solute species. In fitting the depth profile of one solute an error in the irrigation coefficient may be hidden by introducing a compensatory error in the reaction rate term. When the value of the irrigation coefficient is transferred to the equations of the other species, however, the error will become apparent, because it is unlikely that exactly the same compensatory error can be built into the reaction terms of all the species. The same is true for rate constants that appear in more than one continuity equation. Thus, the coupled nature of biogeochemical reactions in sediments imposes stringent constraints on the validity of both the model and the set of model parameters.

Numerical calculation.—The calculations were performed over a total depth of 20 cm, using 400 nodes separated by a constant interval of 0.05 cm. On the order of 3000 iterations were required for convergence of the numerical solution. The computation time on a SUN Sparc Station IPX was approx 30 min.

Organic matter oxidation.—Canfield and others (1993) have determined the depth distributions of the rates of organic carbon oxidation at the three sites studied by combining direct measurements of rates of ΣCO_2 production, NH_4^+ liberation, and $^{35}SO_4^{2-}$ reduction in sediment incubation experiments, with estimates of the total, depth-integrated carbon oxidation rates derived from measurements of the oxygen uptake rate by intact cores. The distribution of the net organic carbon oxidation rate at site S_4 is shown in figure 1. The rates can be fitted to an exponential relationship of the form:

$$R_C = R_o \exp(-\beta x) \tag{107}$$

where R_o and β are positive constants (table 6). Because the carbon oxidation rate distribution is known at the site, relationship (107) was used directly as input for the model. This eliminates the need for solving a separate conservation equation for organic carbon.

With the net rate of carbon oxidation as forcing function, the model calculates the distribution of the various organic matter decomposition pathways (eqs 1-6). The model results for site S_4 are presented in figure 2 and table 7. The depth distributions in figure 2 show considerable vertical overlap between the pathways of organic matter decomposition. Denitrification occurs entirely within the aerobic portion of the sediment, and sulfate reduction extends well into the zone of dissimilatory metal (hydr)oxide reduction. Furthermore, the onset of dissimilatory manga-

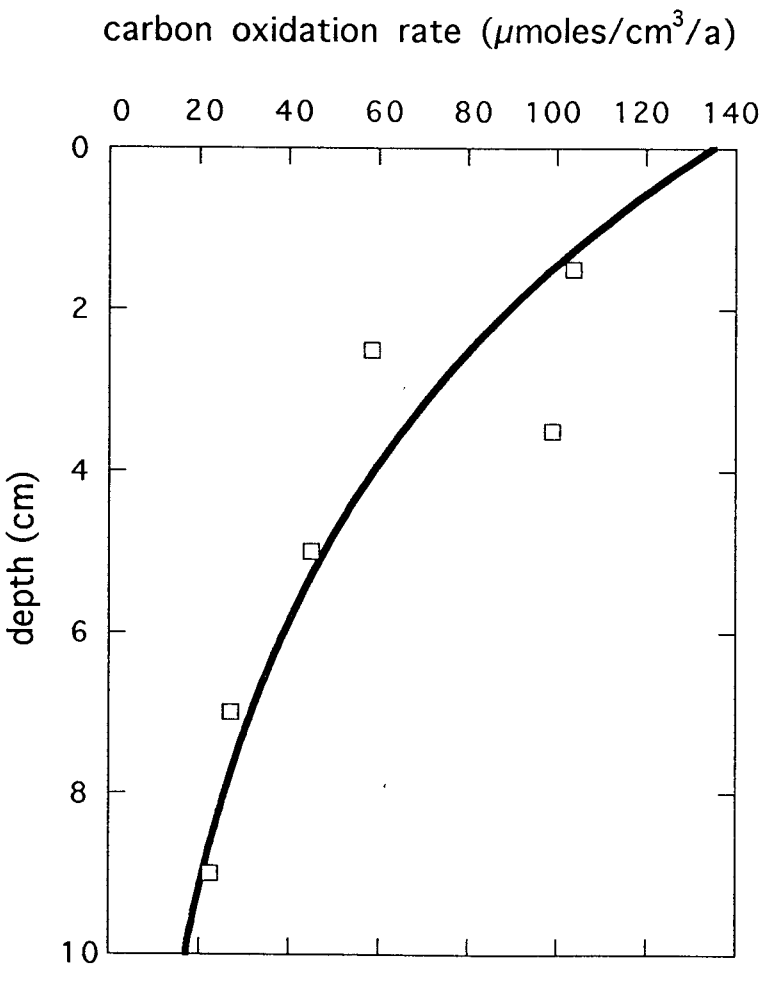

Fig. 1. Rates of organic carbon oxidation as a function of depth, at site S_4. The data are from Canfield and others (1993). An exponential function (eq 107 in text) is fitted through the data points. The function is used as forcing function for the model.

nese coincides with, rather than precedes, the onset of dissimilatory iron reduction.

The large degree of overlap between the oxidation reactions of organic matter is apparent in the data collected at the site, as discussed by Canfield and his coworkers. Measurements by the $^{35}SO_4^{2-}$ incubation method, for instance, provide direct evidence for high rates of sulfate reduction in close proximity to the water-sediment interface (fig. 3), while the absence of measurable pore water nitrate concentrations below the zone of oxygen penetration restricts denitrification to the aerobic

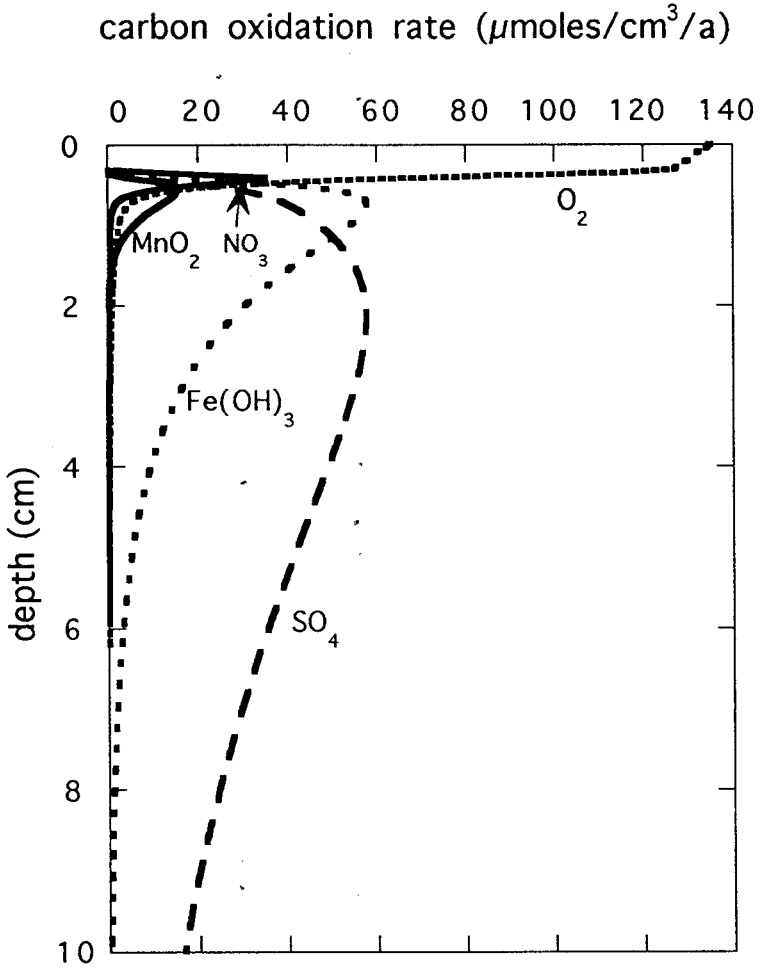

Fig. 2. Model-predicted depth distributions of the organic carbon oxidation pathways (primary redox reactions, table 2). Note the large degree of vertical overlap between the different respiratory pathways.

zone (fig. 4). Similarly, the gradients of the reactive metal (hydr)oxide concentrations (fig. 6) and the results of Mn^{2+} and Fe^{2+} liberation experiments (Canfield, Thamdrup, and Hansen, 1993) argue against a pronounced spatial separation of manganese and iron reduction (see also the discussion in Burdige, 1993).

The picture of organic matter diagenesis that emerges is a very different one from the classical model, where the pathways of organic

TABLE 7

Rates of redox pathways integrated from the water-sediment interface to a depth of 10 cm. The table offers a breakdown of the depth-integrated rates of organic carbon oxidation, manganese reduction, and iron reduction into the competing reaction pathways. The model-calculated rates are compared, where possible, with the estimates of Canfield and others (1993) derived from incubation experiments. All the rates are in units of μmol cm^{-2} yr^{-1}. The numbers in parentheses express the contributions of the pathways as percentages of the total rates

Pathway	Model		Canfield and others	
C_{org} oxidation	572.7	(100)	577.0	(100)
O_2	63.8	(11.1)	77.0	(13.3)
NO_3	7.7	(1.3)	18.2	(3.2)
Mn(IV)	8.3	(1.5)	≥0	(0)
Fe(III)	123.2	(21.5)	186.1	(32.2)
SO_4	369.7	(64.6)	295.7	(51.2)
C_{org}	0	(0)	0	(0)
Mn(IV) reduction	69.8	(100)		
C_{org}	16.5	(23.6)		
Fe^{2+}	52.5	(75.2)		
H_2S	0.8	(1.1)		
Fe(III) reduction	690.6	(100)		
C_{org}	492.8	(71.4)		
H_2S	197.8	(28.5)		

matter oxidation succeed one another in a series of well-defined depth zones (Froelich and others, 1979; Jahnke, Emerson, and Murray, 1982; Ingall and Van Cappellen, 1990; Tromp, Van Cappellen, and Key, 1995). Our earlier modeling work has shown that the separation of the oxidation reactions improves progressively with decreasing rate of net carbon oxidation. Under conditions such as those encountered in the deep-sea, little vertical overlap remains between the respiratory pathways (Van Cappellen and Wang, 1995).

The values for the limiting concentrations, $[EA]_{lim}$, of the dissolved oxidants (O_2, NO_3^-, and SO_4^{2-}) used in the simulations agree with values reported in other studies (table 6). No data exist to which we can compare the limiting concentrations for the solid oxidants. However, the fairly large value of $[EA]_{lim}$ for microbially reducible $Fe(OH)_3$ is consistent with the observed persistence of amorphous Fe(III) in anoxic sediments (Lovely, 1991; Wersin and others, 1991). In contrast, oxidized manganese phases appear to be efficiently and completely reduced below the aerobic surface layer of sediments (Canfield, Thamdrup, and Hansen, 1993). This is reflected by the lower $[EA]_{lim}$ value for MnO_2.

The model-calculated contributions of the different pathways of organic carbon oxidation compare favorably with those derived by Canfield and others (1993) from sediment incubation data and measured

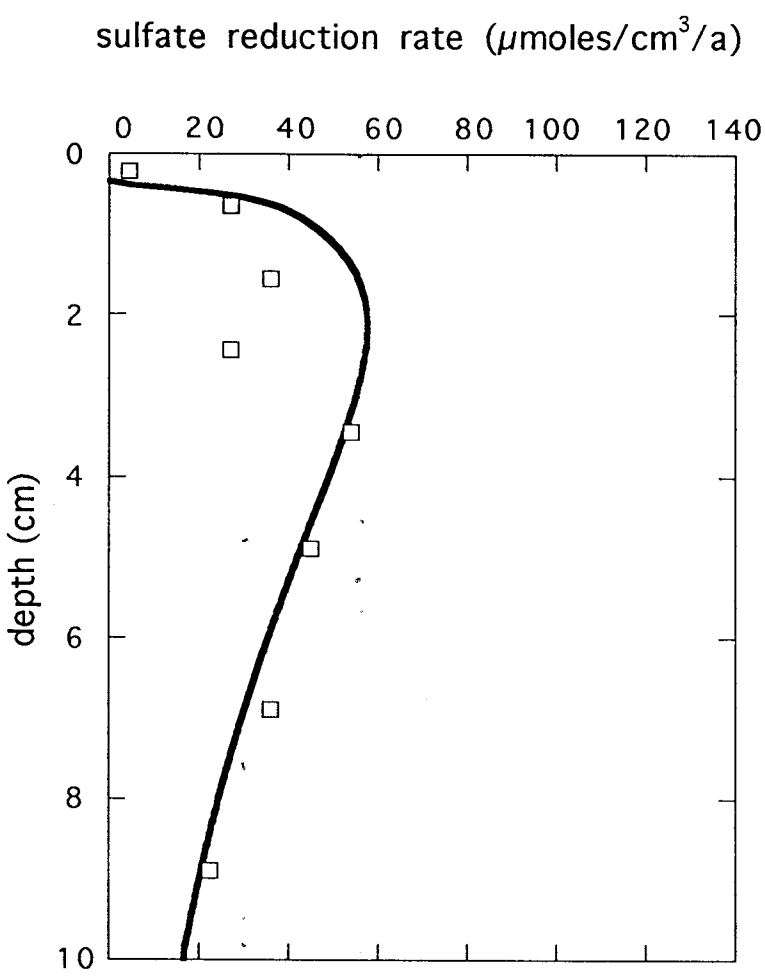

Fig. 3. Sulfate reduction rates as a function of depth. The symbols correspond to rates measured with the $^{35}SO_4^{2-}$ incubation method (Canfield and others, 1993). The curve is the model-predicted distribution, also shown in figure 2. The sulfate reduction rates are expressed in units of mass carbon oxidized.

reactive species distributions (table 7). Both the computational and experimental results indicate a significant role of microbial Fe (hydr)oxide reduction in the oxidation of organic matter at this site. Also, the largest fraction of the oxygen uptake by the sediment appears to be diverted to the oxidation of secondary reduced species, rather than to the direct oxidation of organic carbon.

Bioturbation and irrigation.—The calculated concentration profiles of solid constituents in the top 10 cm of sediment were found to be very

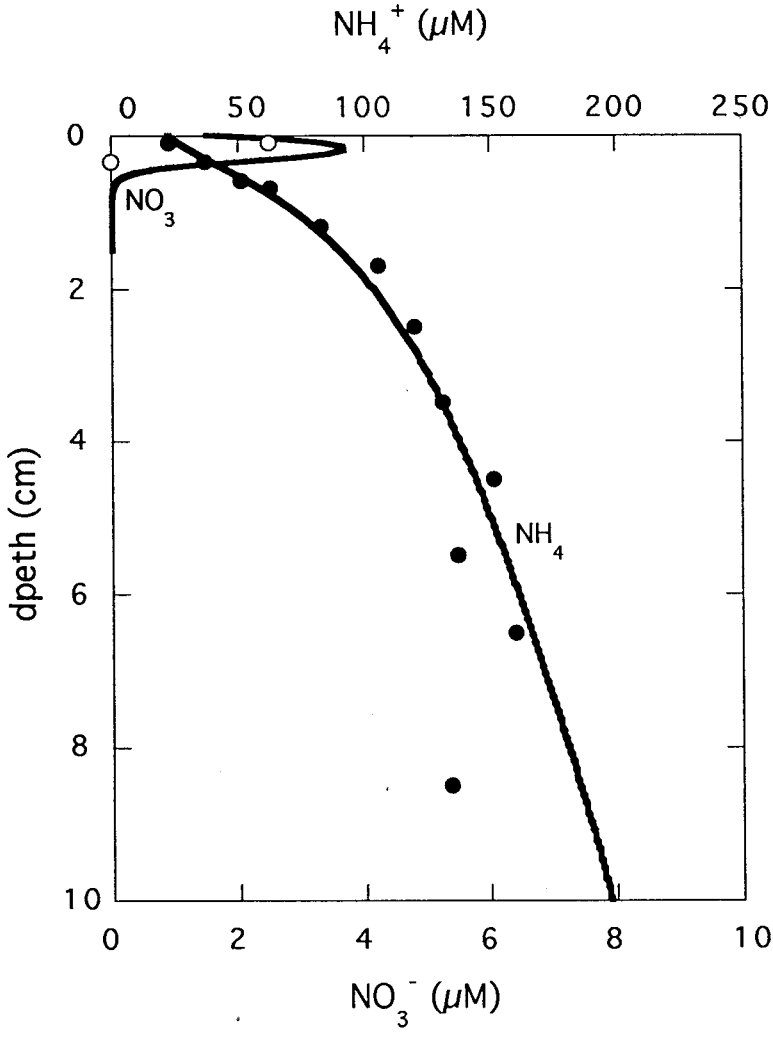

Fig. 4. Measured and calculated pore water distributions of nitrate and ammonia. The depth profile of ammonia was used to constrain the intensity of irrigation in the sediment (see text).

sensitive to the rates of particle mixing. When considered collectively, the depth profiles of the solid species only allow for a fairly narrow range of D_{mix} values. The value used in the simulations (20 $cm^2\ yr^{-1}$) agrees with values reported in the literature for marine depositional environments with similar sedimentation rates (Van Cappellen, Gaillard, and Rabouille, 1993; Tromp, Van Cappellen, and Key, 1995).

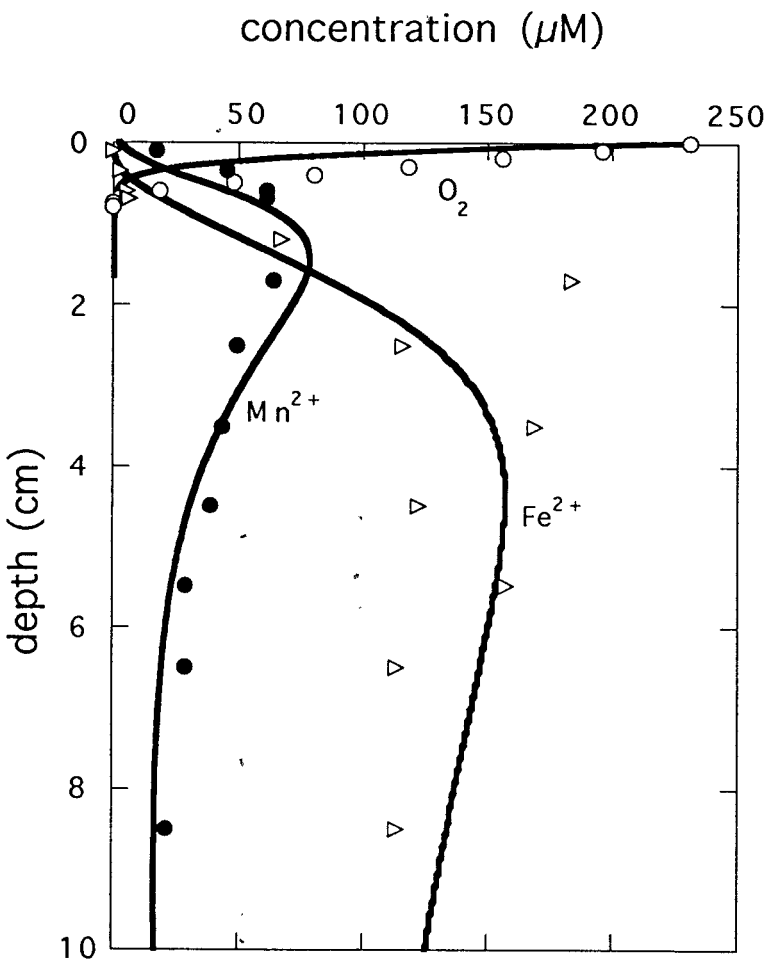

Fig. 5. Measured and calculated distributions of oxygen, manganese(II) and iron(II). The vertical separation in the build-up of pore water Mn^{2+} and Fe^{2+} is attributed partly to the oxidation of Fe^{2+} by manganese oxides.

In the simulations, a simple depth distribution was used for the particle mixing coefficient. From the water-sediment interface down to the lower boundary at a depth of 20 cm, D_{mix} is assumed constant. Other depth distributions were tested. In particular, we compared the constant D_{mix} distribution to gradually decreasing D_{mix} models. All distributions were equally successful in reproducing the solid state profiles measured in the sediment cores. In other words, the available data for site S_4 does not permit a full performance assessment of the different particle mixing models.

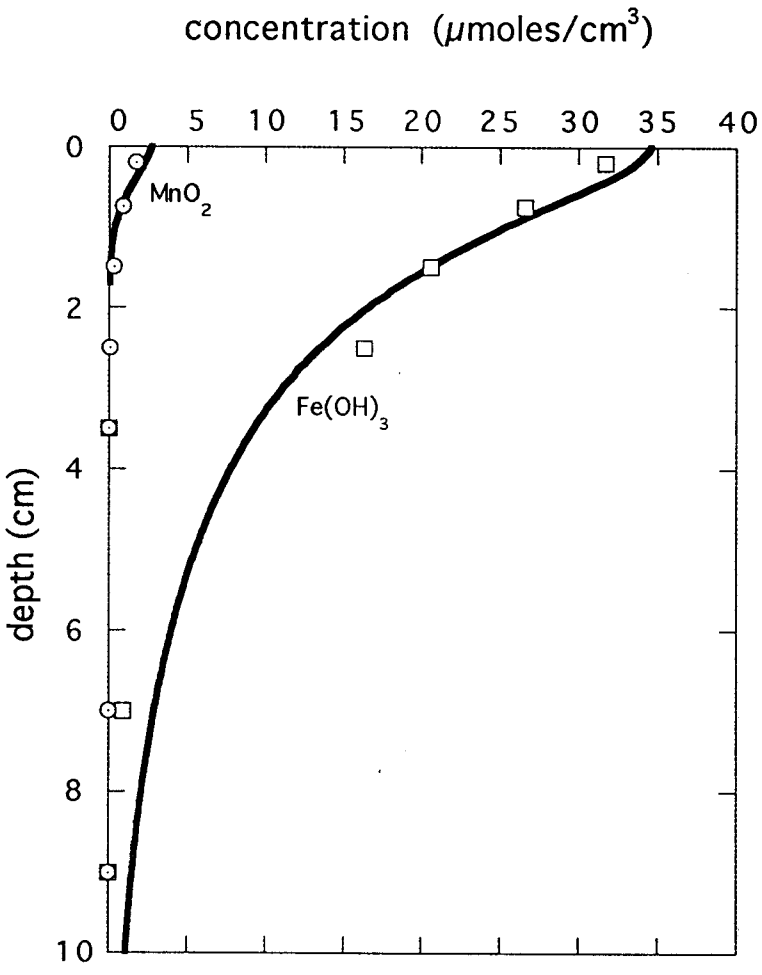

Fig. 6. Measured and calculated distributions of reactive manganese and iron (hydr)oxides. The measured concentrations of reactive (hydr)oxides were obtained by subtracting the background levels of solid phase Mn and Fe(III), measured in the bottom of the cores, from the total extractable concentrations.

The intensity of irrigation was determined primarily from the pore water ammonia profile. The rate of ammonia production in the anaerobic portion of the sediment is constrained by the net rate of carbon oxidation (eq 107) and the C:N ratio of decomposing organic matter. Furthermore, the value of the adsorption constant of ammonia in silty to clayey coastal sediments is restricted to a fairly narrow range (table 6). Thus, the major unknown parameter in the conservation equation of ammonia is the irrigation coefficient (eq 73).

The best match between calculated and measured ammonia profiles were obtained by assuming that the irrigation coefficient decays exponentially according to,

$$\alpha_x = \alpha_0 \exp(-\alpha_1 x) \tag{108}$$

where α_0 and α_1 are positive constants. Martin and Banta (1992) have successfully used eq (108) to model the depth dependence of irrigation rates measured on cores from Buzzards Bay, Massachusetts, using tracer distributions of pore water bromide and $^{222}Rn/^{226}Ra$ disequilibrium. The values of α_0 and α_1 we obtained by fitting the ammonia profile (fig. 4; table 6) fall within the ranges reported by Martin and Banta for their experiments.

In the model, the same irrigation coefficient is applied to all solute distributions, which implies that the walls of the burrows are equally permeable to all the dissolved species (Aller, 1983). This is an assumption requiring further investigation. Nevertheless, given the various constraints on the reaction rates and transport fluxes, all pore water species distributions consistently point to a large effect of irrigation in the upper centimeters of the sediment.

The calculated solute fluxes across the water-sediment interface are all substantially enhanced by irrigation, in agreement with field and experimental studies (Aller, 1982; Graneli, 1979; McCaffrey and others, 1980; Henriksen, Rasmussen, and Jensen, 1983; Gerino and Stora, 1991; Clavero, Fernandez, and Niell, 1992; Matisoff, 1995). According to the model, molecular diffusion dominates the benthic fluxes of oxygen and nitrate, while irrigation is the principal mechanism transporting dissolved ammonia, iron, and manganese to the water-sediment interface.

Fe and Mn cycling.—The profiles of the pore water and solid sediment species of iron and manganese reflect the distribution of redox conditions in the sediment. The insoluble (hydr)oxides, which dominate in the upper centimeters of the sediment, are replaced by reduced pore water and solid phase Fe(II) and Mn(II) species below the oxygen penetration depth. Intense mixing of the sediment, however, counteracts the establishment of a clear separation of oxidized and reduced species (fig. 9). Reactive iron (hydr)oxides persist at considerable depth in the anaerobic portion of the sediment (fig. 6), while authigenic Fe(II) minerals are present at measurable levels in the aerobic zone (fig. 7).

The reduction of iron and manganese differ in the relative importance of dissimilatory and chemical reduction pathways (table 7). The calculations suggest that more than two thirds of the depth-integrated reduction rate of Fe(III) is due to direct microbial utilization of iron (hydr)oxides as terminal electron acceptor in the oxidation of organic matter. For manganese (hydr)oxides, microbial reduction represents only about one fourth of the total reduction rate. The major pathway for reducing Mn (hydr)oxides is reaction with dissolved Fe^{2+} ions. This

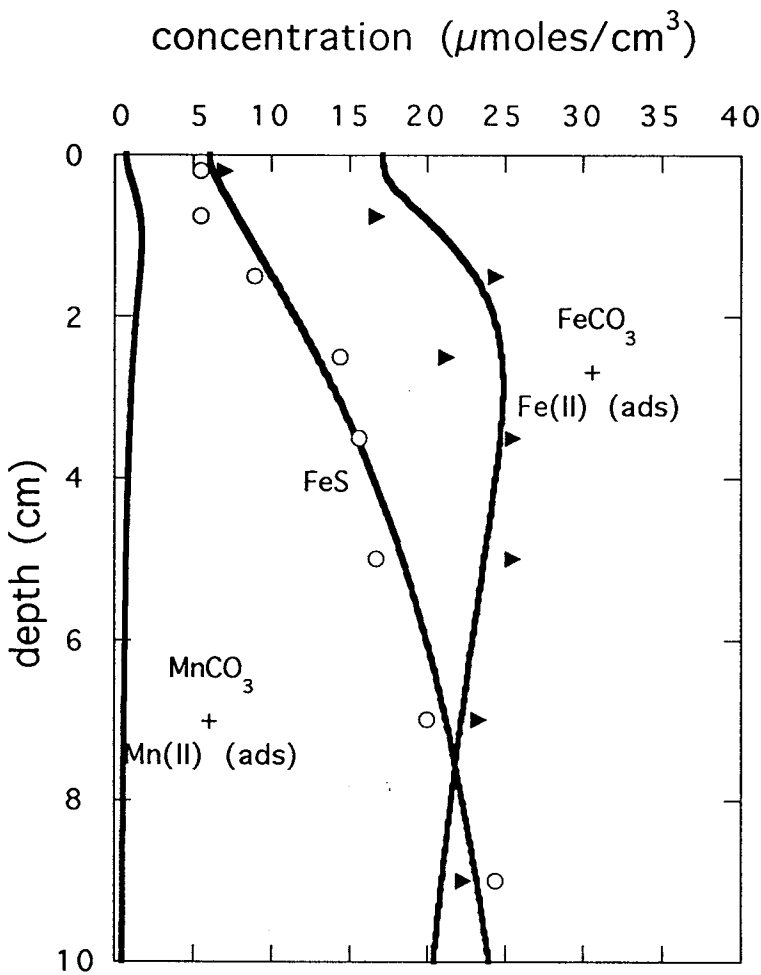

Fig. 7. Distributions of solid phase Mn(II) and Fe(II) species. According to the calculations, authigenic Fe sulfide and Fe/Mn carbonate phases precipitate below the aerobic surface layer. A non-negligible fraction of solid bound Fe(II) is also present as adsorbed Fe^{2+} (see fig. 8).

reaction explains why pore water Fe^{2+} starts building up at a slightly greater depth than Mn^{2+} (fig.5).

One of the reasons why dissimilatory iron reduction is a major reaction pathway in the iron cycle at site S_4 is the presence of excess reducible Fe(III) relative to the reduction capacity of sulfide produced by sulfate reduction. This can be seen by comparing the total rate of iron reduction (691 μmol cm^{-2} yr^{-1}) to the total rate of sulfide production

(185 μmol cm^{-2} yr^{-1}) within the first 10 cm of sediment. Since one mol of sulfide reduces two mols of Fe(III) (see reaction 14), sulfide can at most account for 54 percent of total iron reduction in the surface sediment. In other words, even if all the sulfide were to react with iron (hydr)oxides, there would still be reducible Fe(III) left for microbial respiration. For manganese, on the other hand, the supply of secondary reductants (ferrous iron and sulfide) exceeds the availability of reducible metal. As a result, manganese reducers compete with chemical reduction under far less favorable conditions than iron reducers.

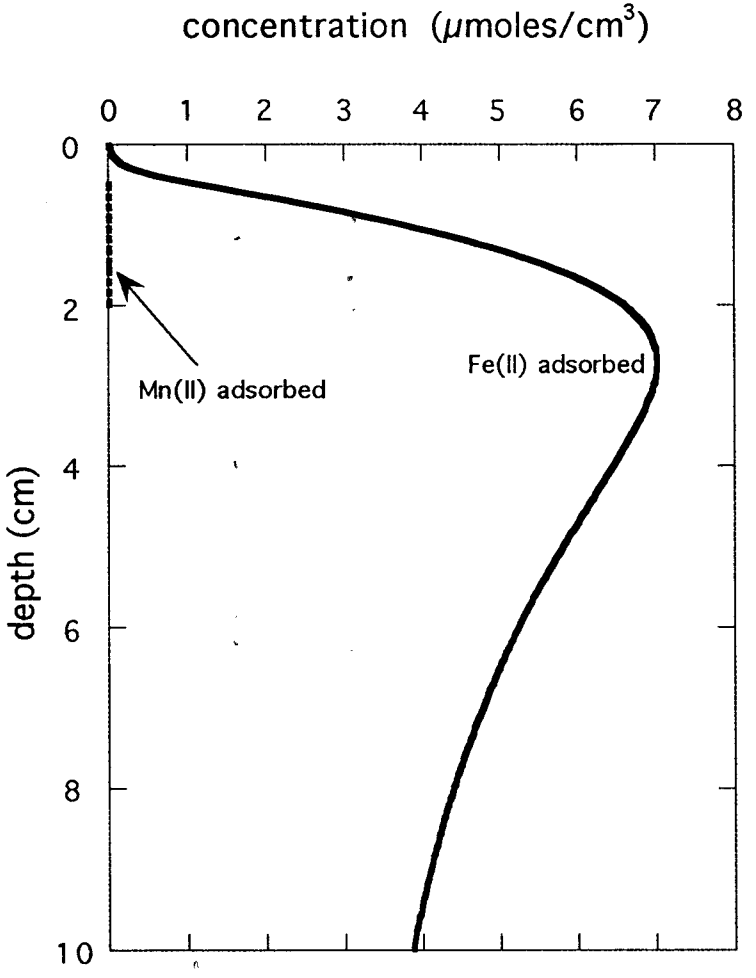

Fig. 8. Model-predicted concentrations of adsorbed Mn^{2+} and Fe^{2+}. The main pathways for oxidation of Mn(II) and Fe(II) in the sediments are reaction between oxygen and the surface-bound cations.

The oxidation pathways of Fe(II) in the surface sediment are, in order of decreasing importance, heterogeneous oxygenation (81 percent), MnO_2 reduction (16 percent), and homogeneous oxygenation (3 percent). Adsorbed Fe(II) is not only an important intermediate in the oxidative precipitation of iron (hydr)oxides, it may also represent a substantial fraction of solid-bound reduced iron (fig. 8). At a depth of 2 cm, the calculated amount of surface-complexed Fe^{2+} accounts for approx 20 percent of total solid phase Fe(II).

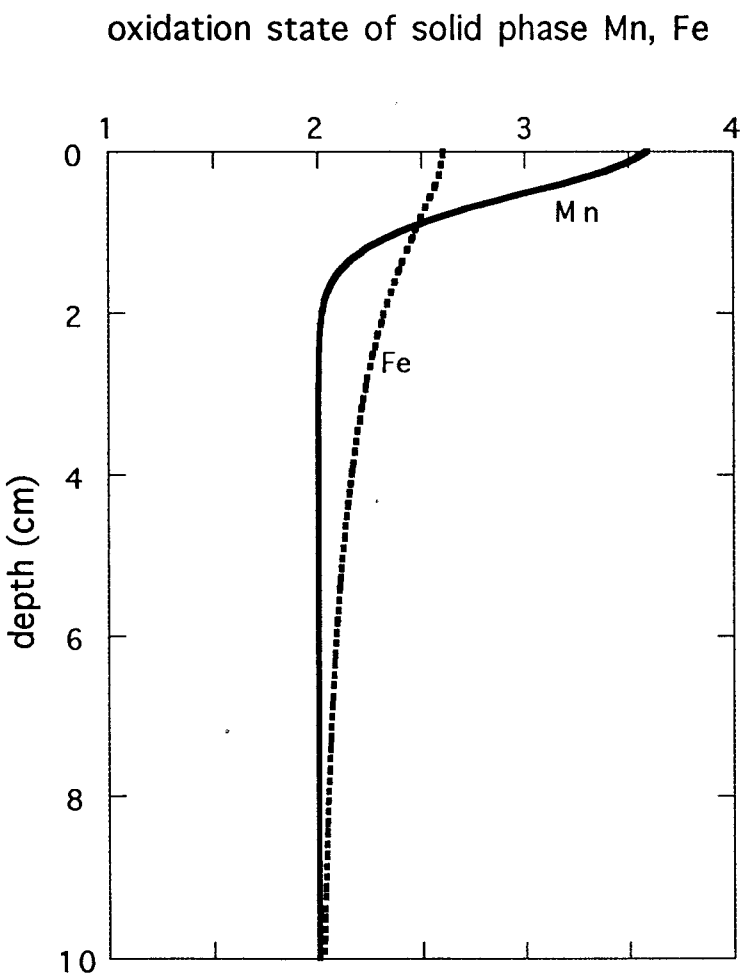

Fig. 9. Calculated distributions of the average oxidation states of reactive solid-bound Mn and Fe. The smooth distributions result from bioturbation which mixes together oxidized and reduced species of the solid phase metals.

The steady state budgets of iron and manganese illustrate the intense benthic recycling of the metals (fig. 12). According to the calculations, only about 1 percent of all Fe(III) cations reduced in the surface sediment are permanently removed to the underlying sediment repository. The remaining Fe(II) cations are reoxidized in the surface sediment, the benthic boundary layer, or the overlying water column. For

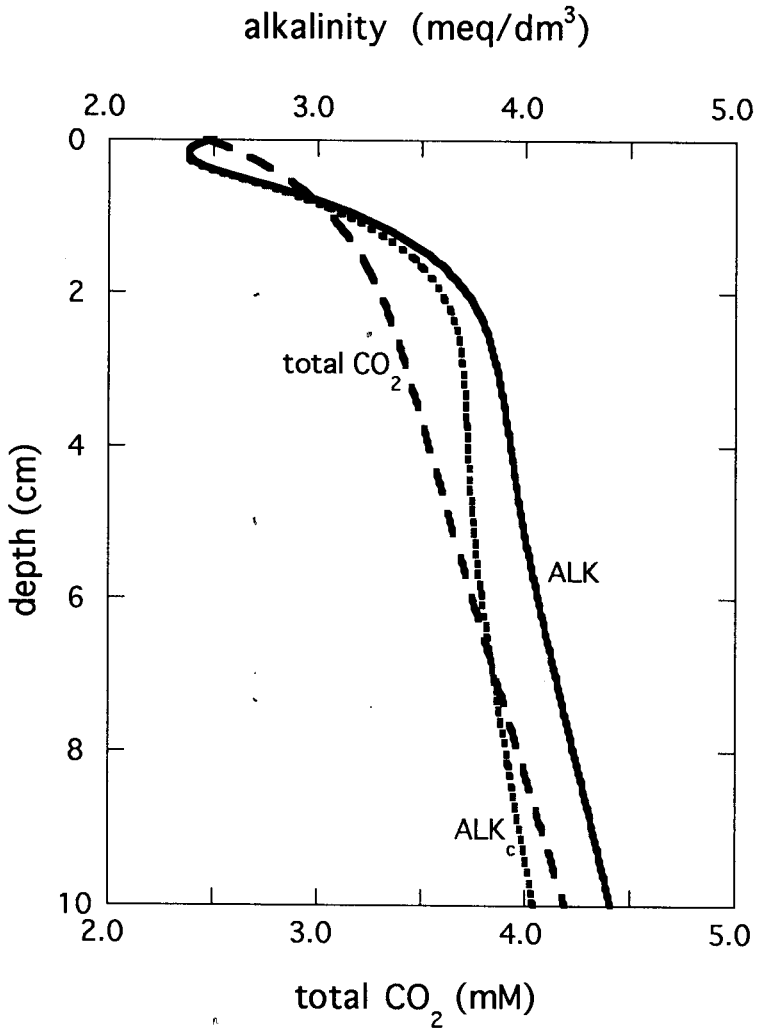

Fig. 10. Calculated profiles of total dissolved inorganic carbon, total alkalinity, and carbonate alkalinity (A) and pH (B). The pH minimum at the bottom of the aerobic zone is caused by the fast redox cycling of Fe and Mn in the surface layer of sediment (see fig. 11).

manganese, burial of solid manganese represents an even smaller fraction (0.2 percent) of the Mn(II) cations produced in the surface sediment. It must be noted that figure 12 shows the burial fluxes of reactive iron and reactive manganese, that is, they do not include the burial of those fractions of Fe and Mn that are unreactive on the time scale of early diagenesis (for example, Fe and Mn bound in silicates and crystalline oxides).

The calculated total fluxes of Fe^{2+} and Mn^{2+} across the water-sediment interface are maximum estimates of the actual fluxes of dissolved metals to the water column (fig. 12). In particular, fast homogeneous oxygenation kinetics may cause part of the Fe^{2+} cations transported

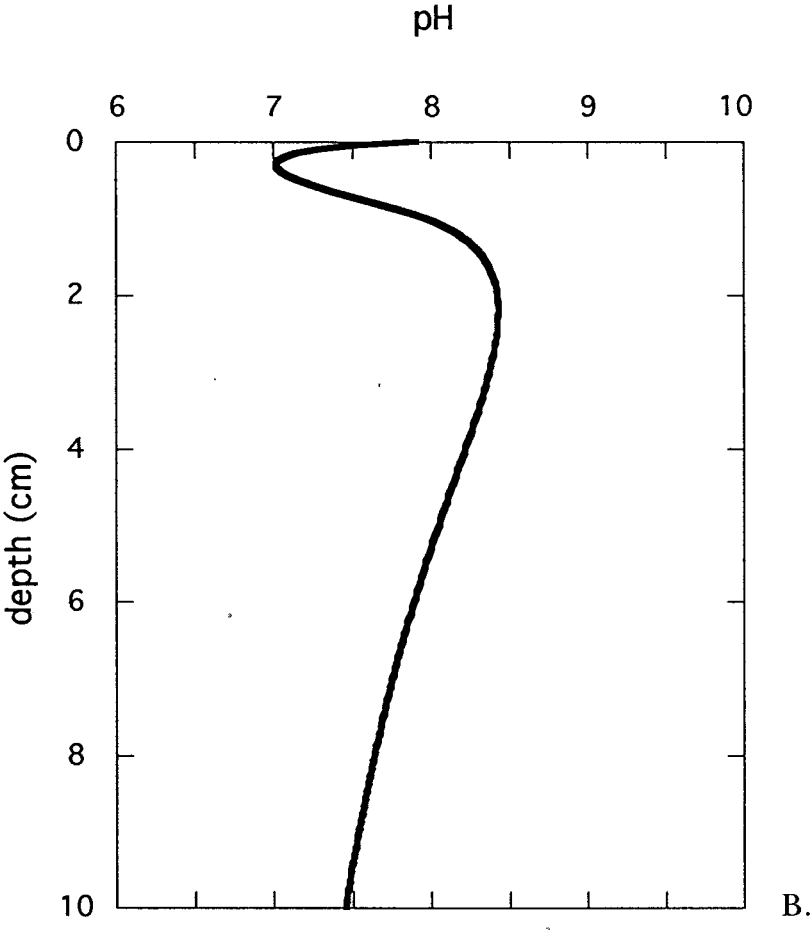

Fig. 10. (continued)

across the water-sediment interface to oxidatively precipitate within the benthic boundary layer and, hence, reduce the flux to the overlying water body (Santschi and others, 1990). Comparison between calculated fluxes and directly measured benthic fluxes would allow to quantify the importance of Fe and Mn retention within the boundary layer.

Pore water pH.—The calculated pore water alkalinity and pH decrease in the upper, aerobic layer of sediment (fig. 10). This is followed by an increase of both parameters in the zone of intense metal (hydr)oxide reduction. Below a depth of 2 cm, the alkalinity continues to rise slowly, while the pH decreases. The general features of the computed pH profile

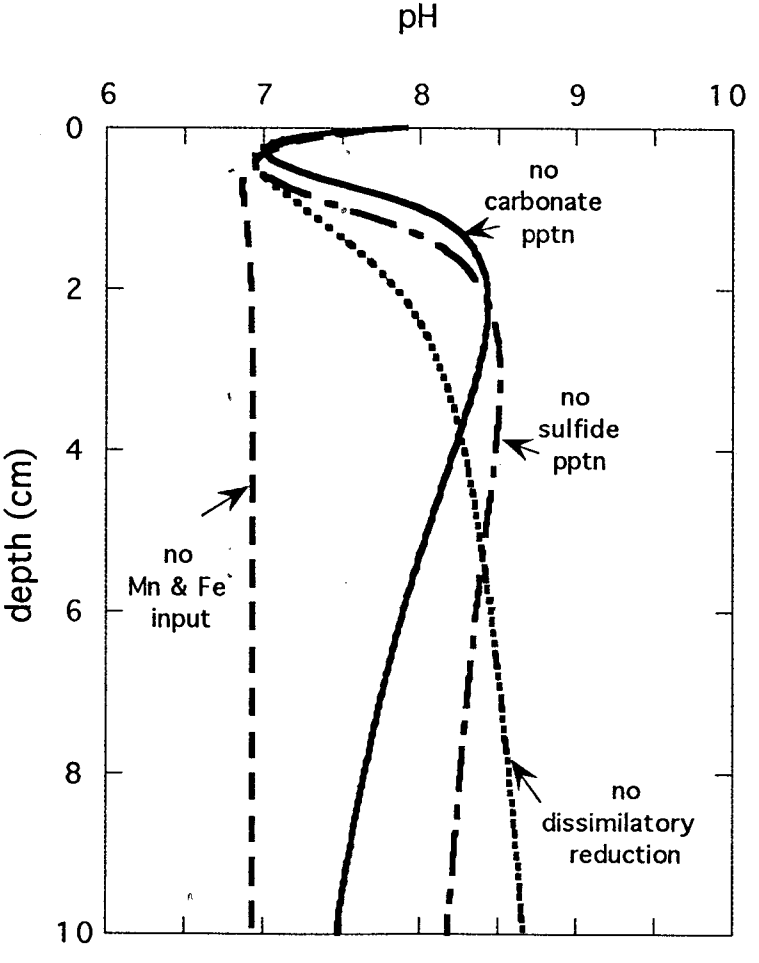

Fig. 11. Calculated pH profiles for a number of different scenarios of Fe/Mn cycling. See text for discussion.

agree with pH measurements made in the Danish coastal sediments (D. Canfield and B. Thamdrup, personal communication).

The model simulations predict substantial variations of pH and alkalinity over fairly short distances in the top sediment. These variations are intimately linked to the cycling of iron and, to a lesser degree, manganese. This is illustrated in figure 11, where the pH profiles computed for a number of different Fe/Mn cycling scenarios are presented. The first scenario corresponds to the complete absence of Fe and Mn in the sediment. The simulation was run by imposing zero deposition fluxes of reactive Fe and Mn at the water-sediment interface. In the second scenario, the dissimilatory pathways of iron and manganese reduction were completely inhibited. In the third and fourth scenarios, we suppressed the precipitation of carbonate minerals and iron sulfide, respectively.

Comparison of the pH profiles in figure 11 shows that dissimilatory and non-dissimilatory oxygen reduction is responsible for the near-surface decrease of pH (and alkalinity). In the absence of iron and manganese, the pH remains nearly constant after its initial drop. All the

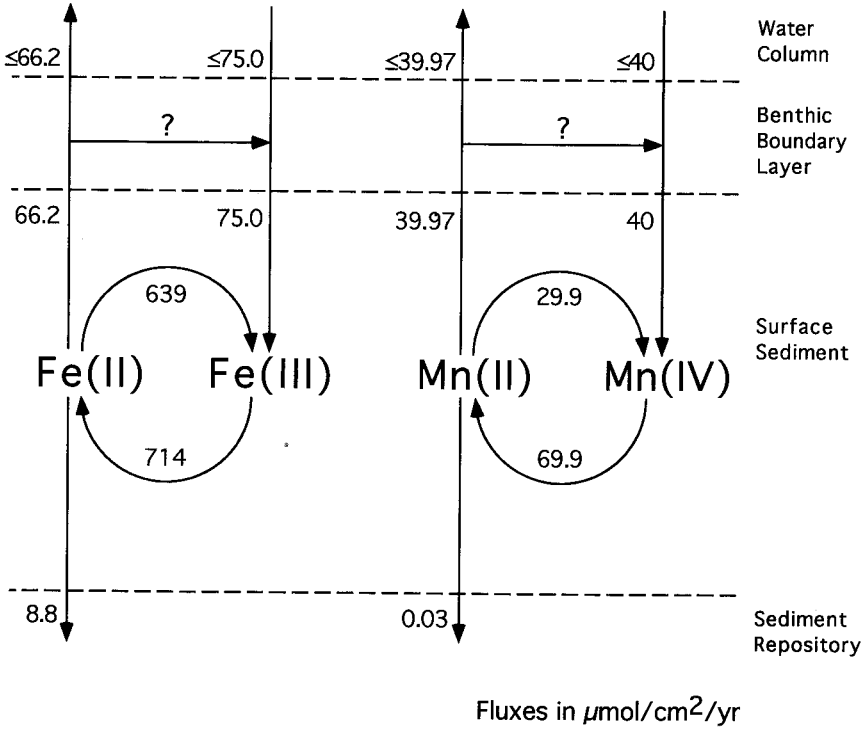

Fig. 12. Calculated steady state budgets of Fe and Mn in the surface sediment (0 to 20 cm) at site S_4.

scenarios that include Fe and Mn show a reversal in the pH profile below the zone of oxygen penetration. When the dissimilatory pathways are inhibited, the lower net rates of reduction of iron and manganese (hydr)oxides result in a slower build-up of pH (and alkalinity) with depth. The precipitation of authigenic mineral phases causes the pH to decrease again below the zone of most intense metal reduction (1-4 cm). At this particular site, iron sulfide precipitation causes a larger drawdown of pH than Fe/Mn carbonate formation.

The model simulations suggest that in rapidly accumulating, organic-rich sediments, such as those found in coastal-estuarine environments and eutrophic lakes, the pH and alkalinity profiles may provide important clues about the early diagenetic cycling of iron and manganese. In particular, a well-developed pH minimum in the near surface sediment may be an indication of rapid redox cycling of the metals across the aerobic-anaerobic boundary.

CONCLUSIONS

The distributions of pore water and solid sediment species of iron and manganese provide a record of the intricate interplay of biogeochemical reactions and transport processes during early diagenesis. As our understanding of the reaction pathways and transport processes advances, it becomes possible to construct mechanistic models that simulate, at an increasingly realistic level, the complex chemical dynamics of Fe and Mn in surface sediments.

In this paper, we have presented a general theory for the quantitative description of the early diagenetic cycling of Fe and Mn. The model treats the sediment as a multi-component reaction-transport system, where the distributions of the reactive species of iron, manganese, carbon, oxygen, sulfur, and nitrogen are coupled to one another through the stoichiometric constraints imposed by the biogeochemical reactions. A finite difference algorithm was developed to solve the coupled conservation equations of the independent chemical species.

The model provides a comprehensive description of the extensive data set collected by Canfield and his colleagues for a marine sediment off the coast of Denmark. The results support the use of the model as an interpretative and predictive tool. Modeling applications include, among others, the quantification of competing reaction pathways, the calculation of elemental budgets, and the derivation of field-based reaction and transport parameters.

Overall, our work demonstrates the feasibility of constructing complex mass balance models that are at par with the current degree of sophistication in field and experimental studies of early diagenetic processes. The increasingly detailed data sets collected in surface sediments, plus the identification of a growing number of potential reaction pathways, require an upgrading of the diagnostic tools used in the interpretation of the data. The development of multi-component transport-reaction models are the logical way to proceed, because these models take

into account the reaction coupling of chemical species which is central to the cycling of elements during early diagenesis.

ACKNOWLEDGMENTS

We wish to thank Don Canfield, Jean-François Gaillard, and an anonymous journal reviewer for their constructive reviews of this paper. We are further indebted to Don Canfield for many enlightening discussions and for sharing his unpublished results on the Danish coastal sediment. Our efforts have also benefited from the comments by Bo Thamdrup. This research was funded by the U.S. Environmental Protection Agency under Cooperative Agreement No. 820813, administered through the Environmental Research Laboratory, Athens, Georgia.

REFERENCES

Aller, R. C., 1982, The effects of macrobenthos on chemical properties of marine sediment and overlying water, *in* McCall, P. L., and Tevesz, M. J. S., editors, Animal-Sediment Relations: The Biogenic Alteration of Sediments: New York, Plenum Press, p. 53–102.

———— 1983, The importance of the diffusive permeability of animal burrow linings in determining marine sediment chemistry: Journal of Marine Research, v. 41, p. 299–322.

———— 1990, Bioturbation and manganese cycling in hemipelagic sediments: Philosophical Transactions of the Royal Society of London, v. A 331, p. 51–68.

———— 1994, The sedimentary cycle in Long Island Sound: Its role as intermediate oxidant and the influence of bioturbation, O_2, and C_{org} flux on diagenetic reaction balances: Journal of Marine Research, v. 52, p. 259–295.

Aller, R. C., and Rude, P. D., 1988, Complete oxidation of solid phase sulfides by manganese and bacteria in anoxic marine sediments: Geochimica et Cosmochimica Acta, v. 52, p. 751–765.

Balistrieri, L. S., Brewer, P. G., and Murray, J. W., 1981, Scavenging residence times of trace metals and surface chemistry of sinking particles in the deep ocean: Deep-Sea Research, v. 28A, p. 101–121.

Balistrieri, L. S., and Murray, J. W., 1982, The surface chemistry of δMnO_2 in major ion seawater: Geochimica et Cosmochimica Acta, v. 46, p. 1041–1052.

Berner, R. A., 1964, An idealized model of dissolved sulfate distribution in recent sediments: Geochimica et Cosmochimica Acta, v. 28, p. 1497–1503.

———— 1970, Sedimentary pyrite formation: American Journal of Science, v. 268, p. 1–23.

———— 1980, Early Diagenesis: A Theoretical Approach: Princeton, New Jersey, Princeton University Press, 241 p.

———— 1984, Sedimentary pyrite formation: An update: Geochimica et Cosmochimica Acta, v. 48, p. 605–615.

Billen, G., 1982, An idealized model of nitrogen recycling in marine sediments: American Journal of Science, v. 282, p. 512–541.

Boudreau, B. P., 1984, On the equivalence of non-local and radial-diffusion models for porewater irrigation: Journal of Marine Research, v. 42, p. 731–735.

Boudreau, B. P., and Canfield, D. E., 1988, A provisional model for pH in anoxic pore waters: Application to the FOAM site: Journal of Marine Research, v. 46, p. 429–455.

Boudreau, B. P., and Westrich, J. T., 1984, The dependence of bacterial sulfate reduction on sulfate concentration in marine sediments: Geochimica et Cosmochimica Acta, v. 48, p. 2503–2516.

Burdige, D. J., 1993, The biogeochemistry of manganese and iron reduction in marine sediments: Earth-Science Reviews, v. 35, p. 249–284.

Burdige, D. J., Dhakar, S. P., and Nealson, K. H., 1992, The role of manganese oxide mineralogy on microbial and chemical manganese reduction: Geomicrobiology Journal, v. 10, p. 27–48.

Burdige, D. J., and Gieskes, J. M., 1983, A pore water/solid phase diagenetic model for manganese in marine sediments: American Journal of Science, v. 283, p. 29–47.

Burdige, D. J., and Nealson, K. H., 1986, Chemical and microbiological studies of sulfide-mediated manganese reduction: Geomicrobiology Journal, v. 4, p. 361–387.

Canfield, D. E., and Berner, R. A., 1987, Dissolution and pyritization of magnetite in anoxic marine sediments: Geochimica et Cosmochimica Acta, v. 51, p. 645–659.

Canfield, D. E., Jørgensen, B. B., Fossing, H., Glud, R., Gundersen, J., Ramsing, N. B., Thamdrup, B., Hansen, J. W., Nielsen, L. P., and Hall, P. O. J., 1993, Pathways of organic carbon oxidation in three continental margin sediments: Marine Geology, v. 113, p. 27–40.

Canfield, D. E., Raiswell, R., and Bottrell, S., 1992, The reactivity of sedimentary iron minerals toward sulfide: American Journal of Science, v. 292, p. 659–683.

Canfield, D. E., Thamdrup, B., and Hansen, J. W., 1993, The anaerobic degradation of organic matter in Danish coastal sediments: Iron reduction, manganese reduction, and sulfate reduction: Geochimica et Cosmochimica Acta, v. 57, p. 3867–3883.

Cantrell, K. J., Serkiz, S. M., and Perdue, E. M., 1990, Evaluation of acid neutralizing capacity data for solutions containing natural organic acids: Geochimica et Cosmochimica Acta, v. 54, p. 1247–1254.

Chapelle, F. H., 1993, Ground-Water Microbiology and Geochemistry: New York, John Wiley, 424 p.

Clavero, V., Fernandez, J. A., and Niell, F. X., 1992, Bioturbation by *Nereis* sp. and its effects on the phosphate flux across the sediment-water interface in the Palmones River estuary: Hydrobiologia, v. 235/236, p. 387–392.

Davis, J. A., and Kent, D. B., 1990, Surface complexation modeling in aqueous geochemistry, *in* Hochella, M. F. and White, A. H., editors, Mineral-Water Interface Geochemistry: Reviews in Mineralogy 23, p. 177–260.

Davison, W., 1991, The solubility of iron sulfides in synthetic and natural waters at ambient temperature: Aquatic Sciences, v. 53, p. 309–329.

Davison, W., and Seed, G., 1983, The kinetics of oxidation of ferrous iron in synthetic and natural waters: Geochimica et Cosmochim. Acta, v. 47, p. 67–79.

De Vitre, R. R., Buffle, J., Perret, D., and Baudat, R., 1988, A study of iron and manganese transformations at the O_2/S(-II) transition layer in a eutrophic lake (Lake Bret, Switzerland): A multimethod approach: Geochimica et Cosmochimica Acta, v. 52, p. 1601–1613.

Devol, A. H., Anderson, J. J., Kuivila, K., and Murray, J. W., 1984, A model of coupled sulfate reduction and methane oxidation in the sediments of Saanich Inlet: Geochimica et Cosmochimica Acta, v. 48, p. 993–1004.

DiChristina, T. J., and DeLong, E. F., 1993, Design and application of rRNA-targeted oligonucleotide probes for the dissimilatory iron- and manganese reducing bacterium *Shewanella putrefaciens:* Applied and Environmental Microbiology, v. 59, p. 4152–4160.

Diem, D., and Stumm, W., 1984, Is dissolved Mn^{2+} being oxidized by O_2 in absence of Mn-bacteria or surface catalysis?: Geochimica et Cosmochimica Acta, v. 48, p. 1571–1573.

Dzombak, D. A., and Morel, F. M. M., 1990, Surface Complexation Modeling: New York, Wiley, 393 p.

Emerson, S., 1976, Early diagenesis in anaerobic lake sediments: Chemical equilibria in interstitial waters: Geochimica et Cosmochimica Acta, v. 40, p. 925–934.

Emerson, S., Jahnke, R., and Heggie, D., 1984, Sediment-water exchange in shallow water estuarine sediments: Journal of Marine Research, v. 42, p. 709–730.

Emerson, S., Kalhorn, S., Jacobs, L., Tebo, B. M., Nealson, K. H., and Rosson, R. A., 1982, Environmental oxidation rate of manganese(II): Bacterial catalysis: Geochimica et Cosmochimica Acta, v. 46, p. 1073–1079.

Enoksson, V. Sörensson, F., and Graneli, W., 1990, Nitrogen transformations in the Kattegat: Ambio, v. 19, p. 159–166.

Froelich, P. N., Klinkhammer, G. P., Bender, M. L., Luedtke, N. A., Heath, G. R., Cullen, D., and Dauphin, P., 1979, Early oxidation of organic matter in pelagic sediments of the eastern equatorial Atlantic: Suboxic diagenesis: Geochimica et Cosmochimica Acta, v. 43, p. 1075–1090.

Gaillard, J.-F., and Rabouille, C., 1992, Using Monod kinetics in geochemical models of organic carbon mineralization in deep-sea surficial sediments, *in* Rowe, G. T., and Pariente, V., editors, Deep-Sea Food Chains and the Global Carbon Cycle: Dordrecht, The Netherlands, Kluwer Academic Publishers, p. 309–324.

Gaillard, J.-F., Pauwels, H., and Michard, C., 1989, Chemical diagenesis in coastal marine sediments: Oceanologica Acta, v. 12, p. 175–187.

Gerino, M., and Stora, G., 1991, *In vitro* quantitative analysis of the bioturbation induced by the polychaete *Nereis diversicolor:* Comptes Rendus de l'Académie des Sciences de Paris, v. 313 (III), p. 489–494.

Graneli, W., 1979, The influence of *Chironomus plumosus* larvae on the exchange of dissolved substances between sediment and water: Hydrobiologia, v. 66, p. 149–159.

Gratton, Y., Edenborn, H. M., Silverberg, N., and Sundby, B., 1990, A mathematical model for manganese diagenesis in bioturbated sediments: American Journal of Science, v. 290, p. 246–262.

Grim, R. E., 1968, Clay Mineralogy: New York, McGraw-Hill, 596 p.

Henriksen, K., Rasmussen, M. B., and Jensen, A., 1983, Effect of bioturbation on microbial nitrogen transformations in the sediment and fluxes of ammonium and nitrate to the overlying water: Environmental Biogeochemistry, v. 35, p. 193–205.

Huyakorn, P. S., and Pinder, G. F., 1983, Computational Methods in Subsurface Flow: Princeton, New Jersey, Princeton University Press, 473 p.

Ingall, E. D., and Van Cappellen, P., 1990, Relation between sedimentation rate and burial of organic phosphorus and organic carbon in marine sediments: Geochimica et Cosmochimica Acta, v. 54, p. 373–386.

Iversen, N. and Jørgensen, B. B., 1985, Anaerobic methane oxidation rates at the sulfate-methane transition in marine sediments from Kattegat and Skagerrak (Denmark): Limnology and Oceanography, v. 30, p. 944–955.

Jahnke, R. A., Emerson, S. R., and Murray, J. W., 1982, A model of oxygen reduction, denitrification, and organic matter mineralization in marine sediments: Limnology and Oceanography, v. 27, p. 610–623.

Jakobsen, R., and Postma, D., 1989, Formation and solid solution behavior of Carhodochrosites in marine muds of the Baltic deeps: Geochimica et Cosmochimica Acta, v. 53, p. 2639–2648.

Johnson, C. A., 1986, The regulation of trace element concentrations in river and estuarine waters contaminated with acid mine drainage: The adsorption of Cu, Zn, P and As on amorphous Fe hydroxides: Geochimica et Cosmochimica Acta, v. 50, p. 2433–2438.

Johnson, K. S., 1982, Solubility of rhodocrosite ($MnCO_3$) in water and seawater: Geochimica et Cosmochimica Acta, v. 46, p. 1805–1809.

Krom, M. D., and Berner, R. A., 1981, The diagenesis of phosphorus in a nearshore marine sediment: Geochimica et Cosmochimica Acta, v. 45, p. 207–216.

Li, Y.-H., and Gregory, S., 1974, Diffusion of ions in sea water and in deep-sea sediments: Geochimica et Cosmochimica Acta, v. 38, p. 703–714.

Lion, L. W., Altmann, R. S., and Leckie, J. O., 1982, Trace-metal adsorption characteristics of estuarine particulate matter: Evaluation of contributions of Fe/Mn oxide and organic surface coatings: Environmental Science and Technology, v. 16, p. 660–666.

Lovley, D. R., 1987, Organic matter remineralization with the reduction of ferric iron: A review: Geomicrobiology Journal, v. 5, p. 375–399.

———— 1991, Dissimilatory Fe(III) and Mn(IV) reduction: Microbiological Reviews, v. 55, p. 259–287.

Luther, G. W., Kostka, J. E., Church, T. M., Sulzberger, B., and Stumm, W., 1992, Seasonal cycling in the salt-marsh sedimentary environment: The importance of ligand complexes with Fe(II) and Fe(III) in the dissolution of Fe(III) minerals and pyrite, respectively: Marine Chemistry, v. 40, p. 81–103.

Lynn, D. C., and Bonatti, E., 1965, Mobility of manganese in diagenesis of deep sea sediments: Marine Geology, v. 3, p. 457–474.

Mackin, J. E., and Aller, R. C., 1984, Ammonia adsorption in marine sediments: Limnology and Oceanography, v. 29, p. 250–257.

Martin, W. R., and Banta, G. T., 1992, The measurement of sediment irrigation rates: A comparison of the Br tracer and $^{222}Rn/^{226}Ra$ disequilibrium techniques: Journal of Marine Research, v. 50, p. 125–154.

Martin, W. R., and Sayles, F. L., 1987, Seasonal cycles of particle and solute transport processes in nearshore sediments: Rn-222/Ra-226 and Th-234/U-238 disequilibrium at a site in Buzzards Bay, MA: Geochimica et Cosmochimica Acta, v. 51, p. 927–943.

Matisoff, G., 1995, Effects of bioturbation on solute and particle transport in sediments, *in* Allen H., editor, Metal Speciation and Contamination of Aquatic Sediments: Chelsea, Lewis, in press.

McCaffrey, R. J., Myers, A. C., Davey, E., Morrison, G., Bender, M., Luedtke, N., Cullen, E., Froelich, B., and Klinkhammer, 1980, The relation between pore water chemistry and benthic fluxes of nutrients and manganese in Narragansett Bay, Rhode Island: Limnology and Oceanography, v. 25, p. 31–44.

McNichol, A. P., Lee, C., and Druffel, R. R. M., 1988, Carbon cycling in coastal sediments: 1. A quantitative estimate of the remineralization of organic carbon in the sediments of Buzzards Bay, MA: Geochimica et Cosmochimica Acta, v. 52, p. 1531–1543.

Michard, G., 1971, Theoretical model for manganese distribution in calcareous sediment: Journal of Geophysical Research, v. 76, p. 2179–2186.

Millero, F. J., Hubinger, S., Fernandez, M., and Garnett, S., 1987, Oxidation of H_2S in seawater as a function of temperature, pH, and tonic strength: Environmental Science and Technology, v. 21, p. 439–443.

Millero, F. J., and Schreiber, D. R., 1982, Use of the ion pairing model to estimate activity coefficients of the ionic components of natural waters: American Journal of Science, v. 282, p. 1508–1540.

Millero, F. J., Sotolongo, S., and Izaguirre, M., 1987, The oxidation kinetics of Fe(II) in seawater: Geochimica et Cosmochimica Acta, v. 51, p. 793–801.

Morgan, J. J., Sung, W., and Stone, A., 1985, Chemistry of metal oxides in natural water: Catalysis of the oxidation of manganese(II) by γ-FeOOH and reductive dissolution of manganese(III) and (IV) oxides, *in* Irgolic, K. J. and Martell, A. E., editors, Environmental Inorganic Chemistry: Weinheim, Germany, VCH Publishers, p. 167–184.

Mucci, A., 1988, Manganese uptake during calcite precipitation from seawater: Conditions leading to the formation of a pseudokutnahorite: Geochimica et Cosmochimica Acta, v. 52, 1859–1868.

Murray, J. W., Balistrieri, L. S., and Paul, B., 1984, The oxidation state of manganese in marine sediments and ferromanganese nodules: Geochimica et Cosmochimica Acta, v. 48, p. 1237–1247.

Myers, C. R., and Nealson, K. H., 1988, Microbial reduction of manganese oxides: Interactions with iron and sulfur: Geochimica et Cosmochimica Acta, v. 52, p. 2727–2732.

Nealson, K. H., and Myers, C. R., 1992, Microbial reduction of manganese and iron: New approaches to carbon cycling: Applied and Environmental Microbiology, v. 58, p. 429–440.

Pedersen, T. F., and Price, N. B., 1982, The geochemistry of manganese carbonate in Panama Basin sediments: Geochimica et Cosmochimica Acta, v. 46, p. 59–68.

Postma, D., 1985, Concentration of Mn and separation from Fe in sediments: I. Kinetics and stoichiometry of the reaction between birnessite and dissolved Fe(II) at 10°C: Geochimica et Cosmochimica Acta, v. 49, p. 1023–1033.

Pyzik, A. J., and Sommer, S. E., 1981, Sedimentary iron monosulfides: Kinetics and mechanism of formation: Geochimica et Cosmochimica Acta, v. 45, p. 687–698.

Rabouille, C., and Gaillard, J.-F., 1991, Toward the EDGE: Early diagenetic global explanation: A model depicting the early diagenesis of organic matter, O_2, NO_3, Mn, and PO_4: Geochimica et Cosmochimica Acta, v. 55, p. 2511–2525.

Robbins, J. A., and Callender, E., 1975, Diagenesis of manganese in Lake Michigan sediments: American Journal of Science, v. 275, p. 512–533.

Santschi, P., Höhener, P., Benoit, G., and Buchholtz-ten Brink, M., 1990, Chemical processes at the sediment-water interface: Marine Chemistry, v. 30, p. 269–315.

Schindler, P. W., and Stumm, W., 1987, The surface chemistry of oxides, hydroxides, and oxide minerals, *in* Stumm, W., editor, Aquatic Surface Chemistry: New York, Wiley-Interscience, p. 83–110.

Shimmield, G. B., and Pedersen, T. F., 1990, The geochemistry of reactive trace metals and halogens in hemipelagic continental margin sediments: Aquatic Sciences, v. 3, p. 255–279.

Sigg, L., 1987, Surface chemical aspects of the distribution and fate of metal ions in lakes, *in* Stumm, W., editor, Aquatic Surface Chemistry: New York, Wiley-Interscience, p. 319–349.

Smith, R. W., and Jenne, E. A., 1991, Recalculation, Evaluation, and prediction of surface complexation constants for metal adsorption on iron and manganese oxides: Environmental Science and Technology, v. 25, p. 525–531.

Stanier, R. Y., Adelberg, E. A., and Ingraham, J. I., 1980, General Microbiology (4th ed.): London, The Macmillan Press, 871 p.

Steefel, C. I., and Lasaga, A. C., 1994, A coupled model for the transport of multiple chemical species and kinetic precipitation/dissolution reactions with application to reactive flow in single phase hydrothermal systems: American Journal of Science, v. 294, p. 529–592.

Steefel, C. I., and Van Cappellen, P., 1990, A new kinetic approach to modeling water-rock interaction: The role of nucleation, precursors, and Ostwald ripening: Geochimica et Cosmochimica Acta, v. 54, p. 2657–2677.

Stone, A. T., 1987, Microbial metabolites and the reductive dissolution of manganese oxides: Oxalate and pyruvate: Geochimica et Cosmochimica Acta, v. 51, p. 919–925.

Stumm, W., 1992, Chemistry of the Solid-Water Interface: New York, Wiley-Interscience, 428 p.

Stumm, W., and Lee, G. F., 1961, Oxygenation of ferrous iron: Industrial and Engineering Chemistry, v. 53, p. 143–156.
Stumm, W., and Sulzberger, B., 1992, The cycling of iron in natural environments: Considerations based on laboratory studies of heterogeneous redox processes: Geochimica et Cosmochimica Acta, v. 56, p. 3233–3257.
Sunda, W. G., and Huntsman, S. A., 1990, Diel cycles in microbial manganese oxidation and manganese redox speciation in coastal waters of the Bahama Islands: Limnology and Oceanography, v. 35, p. 325–338.
Sunda, W. G., and Kieber, D. J., 1994, Oxidation of humic substances by manganese oxides yields low-molecular weight organic substrates: Nature, v. 367, p. 62–64.
Sung, W., and Morgan, J. J., 1980, Kinetics and products of ferrous iron oxygenation in aqueous systems: Environmental Science and Technology, v. 14, p. 561–568.
Thamdrup, B., Finster, K., Fossing, H., Hansen, J. W., and Jørgensen, B. B., 1994, Thiosulfate and sulfite distributions in porewater of marine sediments related to manganese, iron, and sulfur chemistry: Geochimica et Cosmochimica Acta, v. 58, p. 67–73.
Tebo, B. M., and Emerson, S., 1985, Effect of oxygen tension, Mn(II) concentration, and temperature on the microbially catalyzed Mn(II) oxidation rate in a marine Fjord: Applied and Environmental Microbiology, v. 50, p. 1268–1273.
Tromp, T. K., Van Cappellen, P., and Key, R. M., 1995, A global model for the early diagenesis of organic carbon and organic phosphorus in marine sediments: Geochimica et Cosmochimica Acta, v. 59, p. 1259–1284.
Van Cappellen, P., and Berner, R. A., 1988, A mathematical model for the early diagenesis of phosphorus and fluorine in marine sediments: Apatite precipitation: American Journal of Science, v. 288, p. 289–333.
Van Cappellen, P., Charlet, L., Stumm, W., and Wersin, P., 1993, A surface complexation model of the carbonate mineral-aqueous solution interface: Geochimica et Cosmochimica Acta, v. 57, p. 3505–3518.
Van Cappellen, P., Gaillard, J.-F., and Rabouille, C., 1993, Biogeochemical transformations in sediments: Kinetic models of early diagenesis, *in* Wollast, R., Mackenzie, F. T., and Chou, L., editors, Interactions of C, N, P, and S Biogeochemical Cycles and Global Change: Berlin, Springer-Verlag, p. 401–445.
Van Cappellen, P., and Wang, Y., 1995, Metal cycling in surface sediments: Modeling the interplay between transport and reaction, *in* Allen H., editor, Metal Contaminated Aquatic Sediments: Chelsea, Ann Arbor Press, p. 21–64.
Wehrli, B., 1990, Redox reactions of metal ions at mineral surfaces, *in* Stumm, W., editor, Aquatic Chemical Kinetics: New York, Wiley-Interscience, p. 311–336.
Wehrli, B., Sulzberger, B., and Stumm, W., 1989, Redox processes catalyzed by hydrous oxide surfaces: Chemical Geology, v. 78, p. 167–179.
Wersin, P., ms, 1990, The Fe(II)-CO_2-H_2O System in Anoxic Natural Waters: Equilibria and Surface Chemistry: Ph. D. thesis, Swiss Federal Institute of Technology, Zürich, 153 p.
Wersin, P., Höhener, P., Giovanoli, R., and Stumm, W., 1991, Early diagenetic influences on iron transformations in a freshwater lake sediment: Chemical Geology, v. 90, p. 233–252.
Wollast, R., 1990, Rate and mechanism of dissolution of carbonates in the system $CaCO_3$-$MgCO_2$, *in* Stumm, W., editor, Aquatic Chemical Kinetics: New York, Wiley-Interscience, p. 431–445.
Yao, W., and Millero, F. J., 1993, The rate of sulfide oxidation by δMnO_2 in seawater: Geochimica et Cosmochimica Acta, v. 57, p. 3359–3365.